university of groningen / faculty of mathematics and natural sciences

University of Groningen

Zernike Institute for Advanced Materials
Optical Condensed Matter Science

Master Thesis

Ultrafast diffraction in correlated materials

Author:
Rolf B. Versteeg

Supervisors:
Dr. R.I. Tobey
Prof. Dr. Ir. P.H.M. Van Loosdrecht

September 2012 - July 2013

To my parents

you know why...

Contents

Chapter 1

Abstract

Two different ultrafast diffraction studies will be presented in this master thesis work. The first part comprises an ultrafast resonant x-ray diffraction study on the helical antiferromagnetic spiral in dysprosium which was carried out at the Advanced Light Source at the Lawrence Berkeley National Lab. The second part discusses our recent efforts to study diffusion properties in the 3D topological insulator Bi_2Se_3 by means of the transient grating technique. Both parts can be read separately from each other.

Ultrafast resonant x-ray diffraction on the AFM helix in Dysprosium In the first part of this thesis an ultrafast resonant diffraction study on the helical antiferromagnetic spiral in dysprosium is presented. This work was conducted at the Advanced Light Source at the Lawrence Berkeley National Lab. An introduction to the ultrafast resonant x-ray diffraction technique is given first, whereafter a study on the ultrafast demagnetization of helical antiferromagnetic order in a Dysprosium thin film is presented. A static temperature dependence was made as an initial characterisation of the sample. This data shows that the helical pitch decreases (bigger turn angle) with increasing temperature. A 1,5eV pulse is applied in the ultrafast study, which decouples the RKKY coupled 4f momenta, giving rise to a demagnetization. Apart from an amplitude decrease of the diffraction peak, a shift in the peak was also found. In order to take into account this shift a fit model is worked out in detail. Fit parameters for the demagnetization time are obtained with this model. Higher temperatures show to give longer demagnetization ($\sim$ 200-600 ps) and longer recovery times ($\sim$ 5-45ns). In line with theory [1] two different fluence demagnetization regimes become apparent.

Carrier dynamics in the 3D topological insulator Bi_2Se_3 In the second part of the thesis our recent efforts to study diffusion properties in the 3D topological insulator Bi_2Se_3 by means of the transient grating technique is discussed. We aim to study carrier, spin and thermal diffusion. An introduction to topological insulators and its relevant properties under investigation is given. An ultrafast reflectivity setup was constructed to measure the fluence and temperature dependence of the carrier relaxation process. The relaxation time increases with decreasing temperature. The fluence dependence at room temperature shows that the relaxation time increases with increasing excited carrier concentration. Relaxation times fall in a window of 1.0ps to 2.0ps for a fluence dependence over a range of 8-40μJ/cm^2. Our recent effort to upgrade the transient grating setup to a more reliable imaging system is discussed afterwards.

Chapter 2

Ultrafast resonant x-ray diffraction on the AFM helix in Dysprosium

2.1 RXRD

2.1.1 Introduction to tr-RXRD

Diffraction is the constructive interference from successive crystallographic planes of a crystalline lattice [2]. Diffraction occurs when the Bragg law is satisfied:

$$n\lambda = 2d \cdot \sin\theta \tag{2.1}$$

This condition can also be described in the Laue picture. In case when the wavevector transfer $\mathbf{q}$ is equal to a reciprocal lattice vector $\mathbf{G}$ then diffraction will occur, i.e. $\mathbf{G} = \mathbf{q} = \mathbf{k}_i - \mathbf{k}_f$. These reciprocal lattice vectors are not only limited to structural order, but also magnetic, orbital and charge order have their own spacings and respective $\mathbf{G}$-vector. In this way x-rays can be used to not only study long-range order like the structural lattice, but also short and long-range order arising from magnetic order, charge order and orbital order in a material.

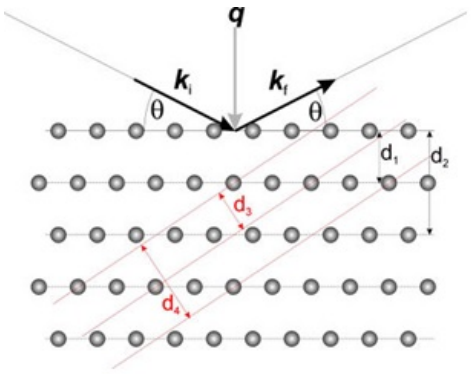

Figure 2.1: Bragg diffraction.

The Bragg condition can also be conveniently written out as:

$$\mathbf{q} = \frac{4\pi}{\lambda}\sin\theta \tag{2.2}$$

where λ is the used x-ray wavelength. The total scattering intensity is given by the sum of the ion structure factor f_{ion} with a phase factor. When the diffraction condition is fulfilled all the ions scatter in phase giving a diffraction signal:

$$I = |\sum_n f_{ion} \cdot e^{(i\mathbf{q}\cdot\mathbf{r})}|^2 \tag{2.3}$$

The structure factor gives the scattering amplitude for an atom and its dependence on $\mathbf{q}$ and x-ray energy $\hbar\omega$. In the most general way the structure factor can be written as:

$$f(\mathbf{q}, \hbar\omega) = f_{non-resonant}(\mathbf{q}) + f_{resonant}(\hbar\omega) + if''(\hbar\omega) \tag{2.4}$$

The first energy-independent term corresponds to classical Thomson scattering, i.e. the scattering of an x-ray by an electron. When one starts to consider an ensemble of electrons, the atom, constructive interference effects starts to set in for the Thomson scattering. This is where the **q**-dependence comes into the picture. When considering an ensemble of atoms, the crystal, the scattering amplitude also starts to depend on the spacing/phase between the atoms. This is where we arrive at the level where interference effects are described by Braggs law above.

The last two terms come into the picture when one tunes the x-ray energy near an absorption edge of the studied material to give *resonant* x-ray diffraction. The absorption edge originates from making a dipole transition between core electron levels and higher lying electronic states. The edges are indicated as K, L, M, etcetera. When the dipole transition happens between bound states, resonance effects are enhanced and the structure factor diverges:

$$f_{resonant}(\hbar\omega) \sim \frac{\sum_n < i|\epsilon|n >< n|\epsilon|i >}{E_{res} - \hbar\omega + i\Gamma/2} \tag{2.5}$$

One can for instance imagine making a L-edge transition from the filled 2s-core orbital to a partly occupied 3d-orbital in a transition metal oxide in order to see spatial variation in the occupation of 3d-orbitals. The resonance enhancement together with the satisfied diffraction condition makes that one scatters from the spatial order under investigation. An example of charge ordering is given in figure 2.2 where a LSNO stripe order phase is shown. The charge order consists of 4 times the structural unit cell in width as spacing and the spin order unit cell spans eight structural unit cells [3].

Let's consider the point where one has found a diffraction peak originating from magnetic order. One can now apply an intense short laser pulse to "melt" the magnetic order. The effect of a laser pulse can give rise to different perturbation mechanisms like lattice heating, dd-transitions, creating charge-transfer transitions between different lattice sites, electronic heating of electrons, etcetera. Now by delaying the time between the pump laser pulse and the probe x-ray pulse one can track the evolution of the melting and the recovery of the order. This is the *time resolved* resonant x-ray diffraction technique.

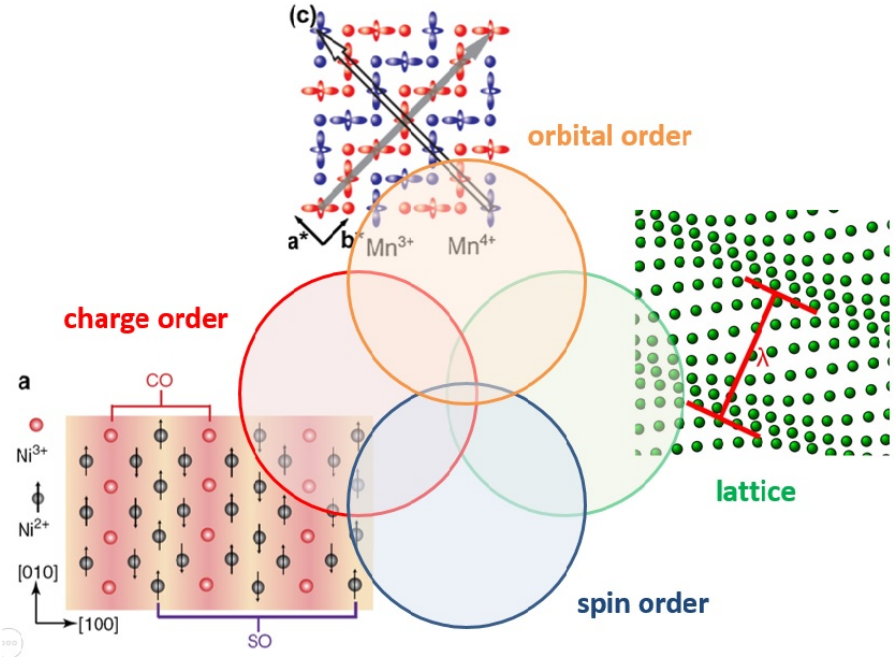

Figure 2.2: The charge, magnetic, orbital and lattice systems of strongly correlated materials have interesting coupling mechanisms between them. With resonant x-ray diffraction one can study the order of these systems, while the order of another coupled system is perturbed by a laser pulse. The charge and spin order are illustrated with the LSNO-unit cell [3], while an example of orbital order is illustrated in PCMO [4].

2.1.2 Experimental considerations

For performing a time resolved resonant x-ray diffraction experiment one needs to have a pulsed x-ray source. The work described in this chapter was performed at the Advanced Light Source synchrotron. This synchrotron emits x-ray pulses (other options for pulsed x-ray sources are free-electron lasers [5] or recently even high-harmonic generation [6]). In the synchrotron ring, relativistic electrons circle around, giving off x-ray radiation since they experience an acceleration when they follow a curved trajectory. The ALS ring is filled with different "electron bunches". In the ring there are 328 so-called "buckets". These buckets are filled according to a specific pattern. There are 2 groups of around 100 buckets with a small electron current. These are the "multi-bunches". In between the multibunches there are two filling gaps. In these empty regions 1 bucket is filled with a high electron current. These high current buckets are the "camshafts". They give a high intensity x-ray pulse, to be more specific, around 70ps. This x-ray pulse is electronically locked in time to an external laser system. Via an electronic delay system the time between the incoming laser pulse and the x-ray pulse can be varied. Both the x-ray pulse and the laser pulse end up in an ultra-high vacuum scattering chamber with a $\theta/2\theta$ diffractometer system. Beamline 6.0.2 works in an x-ray energy range of 250eV to 1,5keV. The beamline is also capable of producing $\sim$ 100fs x-ray pulses by means of the slicing technique [7].The sample is placed in a cryostat sample holder. An avalance photodiode is used to detect the diffraction peak at the 2θ position.

Figure 2.3 gives a schematic overview of the tr-RXRD experimental setup. The lower box gives the schematics of how the incoming laser and x-ray signal look like in time on a fast scope. The signal of one camshaft is gated with a boxcar and only integrated. Now the time between the laser pulse and the gated out x-ray pulse can be varied to obtain the time-dependent x-ray diffraction. A more rigorous explanation of the experimental setup is given in appendix 2.3.1. Also an illustration of a synchrotron filling pattern [8] and the corresponding scope view are given here.

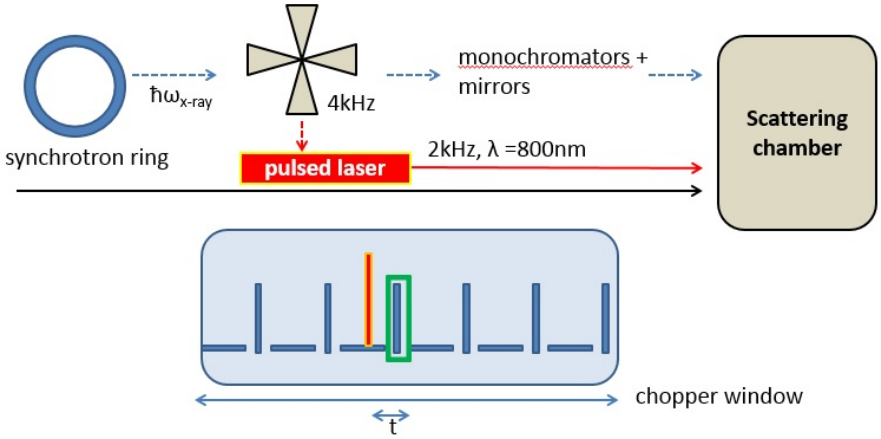

Figure 2.3: Beamline schematics: X-rays come out of the synchrotron in bunches of 70ps. These pass an x-ray chopper to cut down the average flux in order not to damage the sample. Mirrors and monochromators allow to select different energies and pass the x-rays into the scattering chamber. The x-ray chopper gives a trigger pulse to the electronic system which is coupled with a 800nm high-intensity laser. On a chopper window all the incoming signals look schematically like indicated. There are low-intensity multibunches and high intensity camshafts. The laser pulse (red) is electronically locked to a camshaft (by electronics). The signal from this camshaft is boxed (green) and integrated out to get the x-ray intensity.

2.2 Helical antiferromagnetic ordering in dysprosium

2.2.1 Introduction

The heavy rare earth metals from Gd to Tm are paramagnetic at room temperature. At lower temperatures they show diverse and interesting magnetic ordering forms. For this research the ultrafast magnetization dynamics of dysprosium was studied. An epitaxial Y/Dy/Y sample is used [9]. When temperature is lowered, dysprosium undergoes a first order phase transition from the paramagnetic regime to a *helical antiferromagnetic* structure at the Néel temperature T_n ~180K. The turn angle ϕ of the spiral structure decreases continuously upon decreasing the temperature. Stated differently: the *helical pitch* increases with decreasing temperature. Here *helical pitch* is defined as the width of one complete helix turn, measured parallel to the axis of the helix. At the Curie temperature T_c ~80K dysprosium undergoes a first order phase transition to the ferromagnetic phase [10].

2.2.2 Helical magnetic order

Many rare earth metals have an hcp-type crystal structure where the atoms lie in layers. Due to a variation in strength of the exchange interaction between the spins in neighbouring planes and next-neighbouring planes helical magnetic order can appear in these materials [11]. A simple toy model to calculate the turn angle can be easily presented as follows: Let's define a turn angle ϕ between two neighbouring layers with an exchange constant J_1. The next-nearest neighbouring layers then have an angle 2ϕ between them with an exchange constant J_2. The energy for this system then is given by:

$$E = -2NS^2(J_1 \cos\phi + J_2 \cos 2\phi) \tag{2.6}$$

Here N is the number of atoms per plane and S the spin quantum number. Minimizing this energy with respect to ϕ ($\partial E/\partial\phi = 0$) gives three different solutions: $\sin\phi = 0$ (ferromagnetic coupling), $\sin\phi = \pi$ (antiferromagnetic coupling) and $\sin\phi = -J_1/4J_2$. This last solution gives

helical order. Depending on the sign of J_1 and J_2 one gets helical ferromagnetism or helical antiferromagnetism. The latter is the case for dysprosium.

The toy model given above is a gross oversimplification of the real physical mechanism of helical order in rare earth magnets. The coupling between layers in rare earth metals originate in the RKKY-interaction [11]. For dysprosium the RKKY-interaction works as follows: A Dy 4f magnetic moment spin-polarizes a 6s conduction electron. This 6s spin-polarized electron can then have an exchange interaction with another 4f moment. In this way two 4f moments are indirectly exchange coupled via the 6s conduction electron. The sign and amplitude of the RKKY-interaction has an oscillatory amplitude depending on the distances between the magnetic moments, giving rise to a varying exchange constant J.

The spiral length is determined by the properties of the Fermi surface [12, 13]. When two bands crossing the Fermi surface are parallel with respect to each other, the electronic susceptibility of the conduction electrons will diverge at this specific **q**-value between the two bands. The exchange constant is directly proportional to the electronic susceptibility, so $J(\mathbf{q})$ will be maximum where the electronic susceptibility diverges. This instability results in the formation of a spin density wave with wavevector **q**. This phenomenon is called *Fermi surface nesting*. If $q = \pi/c$ then we have antiferromagnetic order. It is however more common that the spin density wave is incommensurate with the lattice. In the next paragraph we will see that for dysprosium the q-value varies between $q \approx \pi/21c$ and $q \approx \pi/15c$, where c is the structural unit cell in the z-direction.

2.2.3 Static temperature dependence

As an initial characterisation of the sample a temperature dependence of the static AFM-diffraction signal is made. From formula 2.23 we know how to calculate the diffraction angle with respect to the chamber coordinate system. The diffraction angle can be calculated into its corresponding q-value according to:

$$n\lambda = 2d\sin\theta = \frac{4\pi}{q}\sin\theta \tag{2.7}$$

$$|q_{AFM}| = \frac{4\pi}{\lambda}\sin\theta = |(00\tau)| \tag{2.8}$$

This q-value can be used to determine the turn angle ϕ_{turn} between the antiferromagnetically coupled dysprosium layers:

$$\phi_{turn} = 180^\circ \cdot |q_{AFM}| = 180^\circ \cdot |(00\tau)| \tag{2.9}$$

The turn angle can be simply used to calculate the corresponding amount of layers in the spiral. These are the heights indicated in figure 2.6:

$$D_{AFM} = \frac{360^\circ}{\phi_{turn}} \tag{2.10}$$

$$D_{spiral} = 2 \cdot \frac{360^\circ}{\phi_{turn}} \tag{2.11}$$

An x-ray energy of E=1338eV, or $\lambda = 9.27\mathring{A}$ was used to fulfill the resonance condition for the AFM peak. The diffraction peak intensity and position was measured as a function of temperature. The temperature was increased from 80K with steps of 10K up to the point that the peak disappears. This happens around 175K. This is where the paramagnetic regime is entered. The temperature dependence of the q-value and the number of layers in a full spiral are shown in figure 2.6. The graphs of the diffraction angle and the number of AFM layers versus temperature are shown in appendix 2.3.2.

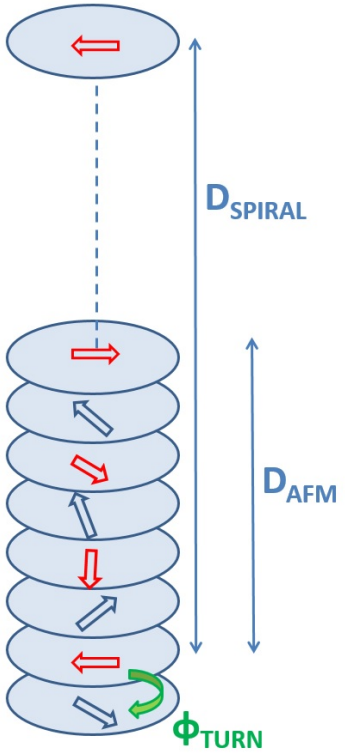

Figure 2.4: Illustration of the spiral accompagnied by the definitions made in the text.

What is conceptually happening when the temperature is increased is shown in figure 2.5 below. Upon heating the $\theta_{AFM,diff}$ increases, which means that the $|q_{AFM}|$ increases. This means that the D_{AFM} is decreasing. This decrease in D_{AFM} can be explained by an increasing turn angle between the AFM layers, so the spiral winds up "faster" with increasing temperature.

$$T \uparrow \Rightarrow \theta_{AFM,diff} \uparrow \Rightarrow |q_{AFM}| = \frac{4\pi}{\lambda} \sin\theta \uparrow \Rightarrow D_{AFM} \downarrow \tag{2.12}$$

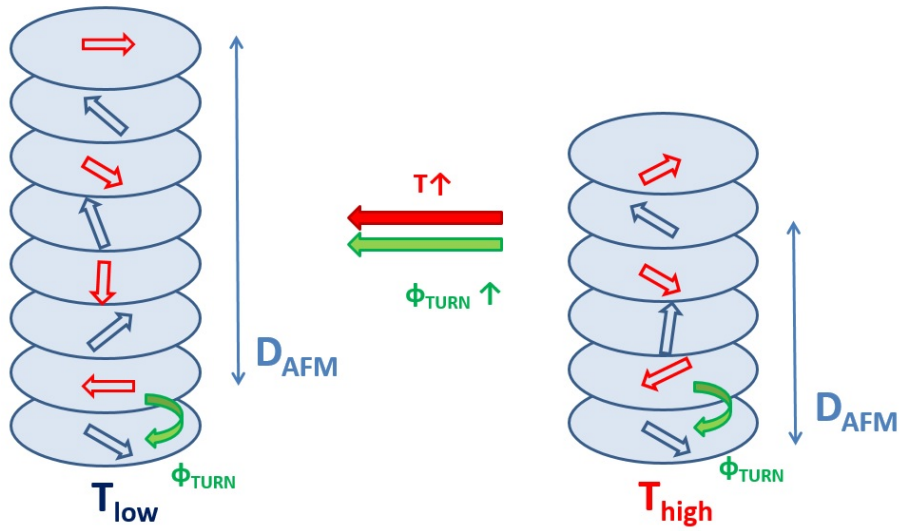

Figure 2.5: Upon heating the ϕ_{turn} angle starts to increase. This gives a decrease in the D_{AFM} spiral lenght.

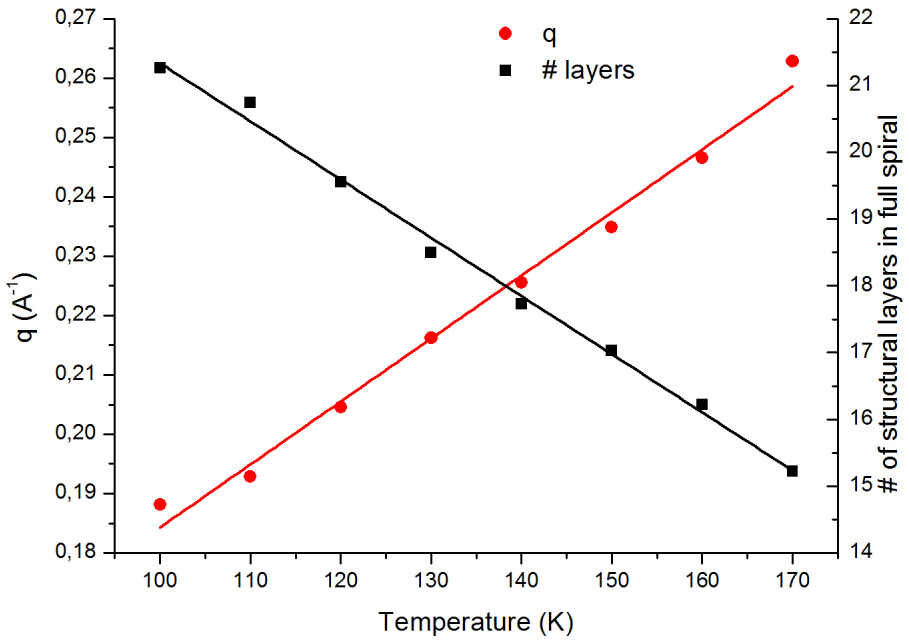

Figure 2.6: Temperature dependence of q-value and the number of structural layers in a full spiral.

2.2.4 Ultrafast dynamics in Dysprosium

In this section pump-probe data on the helical antiferromagnetic diffraction peak will be presented. An excitation of 1,5eV is used to perturb the magnetic order in dysprosium. A fast conceptual insight in what is happening can be described as follows: the 1,5eV excitation will promote the 6s conduction band electrons at the Fermi level to a higher energy in the conduction band. The coupling between the 4f moments is now taken away. This will alter the magnetic order giving rise to a decrease in the AFM peak.

Temperature dependence

In this paragraph the temperature dependence of the demagnetization process is presented. The measurement procedure is as follows: take a $\theta/2\theta$ scan in the unperturbed state, move the motors to the peak and then take a time-trace over a 20ns span. The result of this for a few different temperatures are shown in the figure below. It can be seen that with increasing temperature the demagnetization amplitude becomes bigger. For elevated temperatures the demagnetization signal can even be resolved within the time-resolution of the beamline (bunch lenght $\sim$ 70ps). This data is fitted with an ingrowing and decreasing exponent, convolved with a Gaussian. Temperature dependent fit values of the decay dynamics t_1 and the recovery dynamics t_2 are presented below.

$$I(t) = I_0 \cdot (1 - e^{-t_2/t}) \cdot e^{-t_1/t} \tag{2.13}$$

This fit serves as a rough model of the process after the laser excitation. As we will see, the data needs to be modelled more thoroughly than merely an ingrowing and decaying exponential. The fit above nevertheless gives a good indication of the timescales involved in the demagnetization process.

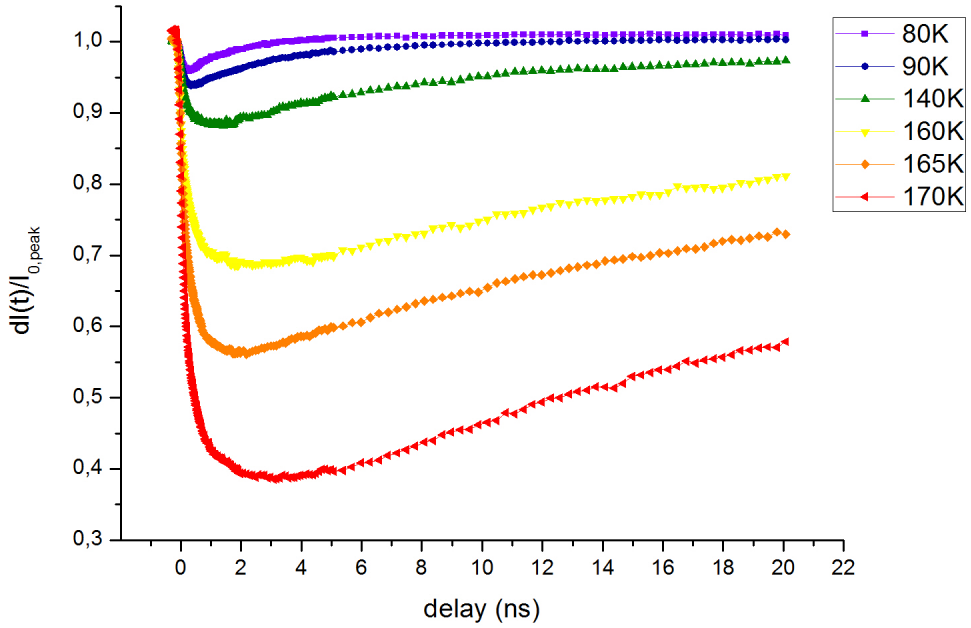

Figure 2.7: Temperature dependent demagnetization traces.

Peak shift fit model

Apart from merely a peak intensity drop one can also expect that the length of the AFM spiral changes upon laser excitation. That this is the case can be easily inferred by making a $\theta/2\theta$ scan in time. In figure 2.9 it is clearly seen that the peak shifts its position in time. This also means that the simple fit in formula 2.13 is not fully valid to interpret the data.

The procedure to take into account the peak shift is illustrated below. Figure 2.10 gives a schematic overview of the procedure as a guide to the eye. The "raw" data consists of a laser-on signal $I(t)$ and a laser-off signal I_0.This will give the relative decrease of the intensity in time which is indicated with $g(t)$. Trivially reworking this expression gives the "clean" time-dependent signal $I(t)$.

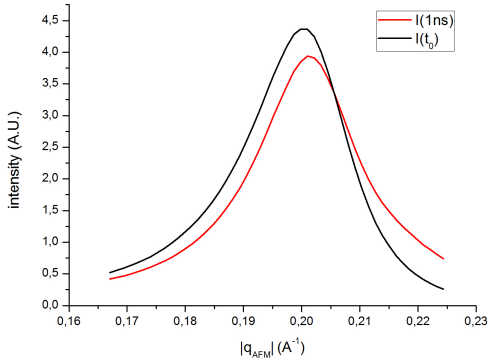

Figure 2.9: By making a $\theta/2\theta$ scan at different time delays one can see that the peak also shifts its q_0 position. $\theta/2\theta$ scans are captured at pre-laser excitation time and t=1ns at 105K.

$$g(t) = \frac{I(t) - I_0}{I_0} \rightarrow I(t) = I_0(g(t) + 1) \tag{2.14}$$

The intensity drop now needs to be measured at both FWHM positions of the peak at t_0. The corresponding q-positions are $q_{high} = q_0(0) + \Gamma$ and $q_{low} = q_0(0) - \Gamma$ where Γ is the FWHM value of the peak.

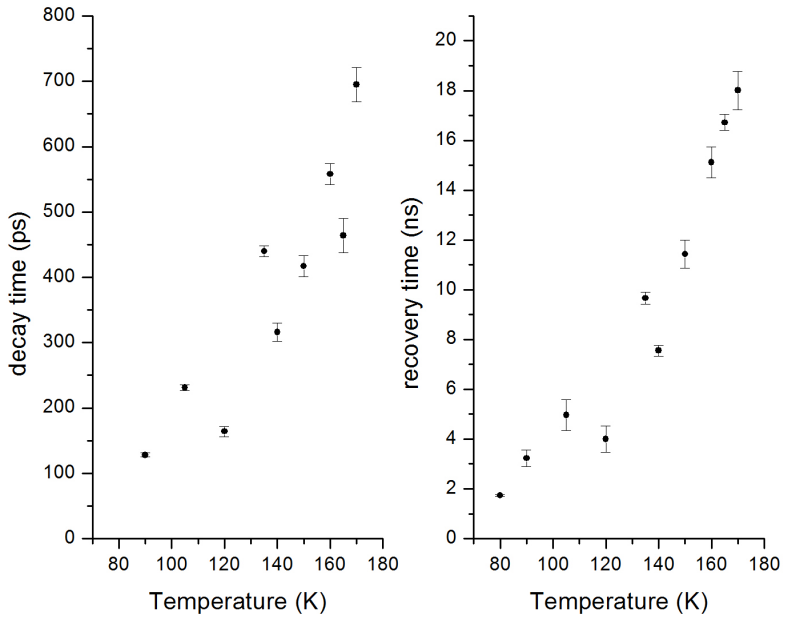

Figure 2.8: Temperature dependent time constants determined according to relation 2.13.

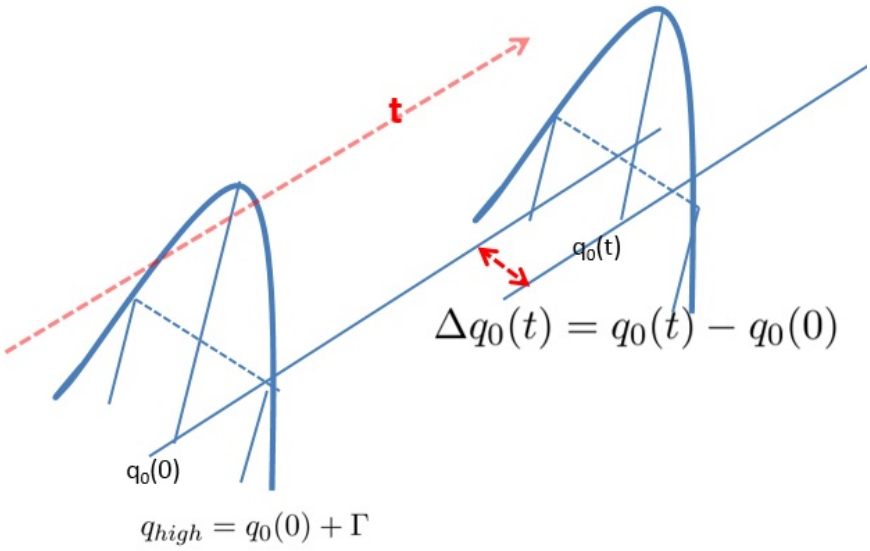

Figure 2.10: The pre-laser excitation diffraction peak (Lorentzian lineshape) has a center $q_0(0)$. After laser excitation the diffraction peak moves to $q_0(t)$. The change in the center in time is indicated with $\Delta q_0(t)$. Γ is the HWHM value of the Lorentzian.

We know that the peak shifts, so q_0 depends on time: $q_0(t)$. Formula 2.15 gives a Lorentzian which has a time-dependent central position. The time-dependent intensity is measured "along" the q-coordinates q_{low} and q_{high} (positions at t=0) and this signal is given by 2.15. $a(t)$ is the q-independent intensity dependence which we are looking for.

$$I(t, q, q_0(t)) = \frac{a(t) \cdot \Gamma^2}{\Gamma^2 + (q - q_0(t))^2} \tag{2.15}$$

Evaluation of the intensity at q_{low} gives:

$$I(t, q = q_{low}, q_0(t)) = \frac{a(t) \cdot \Gamma^2}{\Gamma^2 + (q_0(0) - \Gamma - q_0(t))^2} = \frac{a(t) \cdot \Gamma^2}{\Gamma^2 + (-\Delta q_0(t) - \Gamma)^2} \tag{2.16}$$

The shift in the central position of the Lorentzian is defined as $\Delta q_0(t) = q_0(t) - q_0(0)$. The same can be done for q_{high}. Now one can calculate the ratio between the intensity at both sides of the peak. The analytical expression for this ratio is:

$$K(t) = \frac{I(t, q = q_{low})}{I(t, q = q_{high})} = \frac{\Gamma^2 + (\Gamma - \Delta q_0(t))^2}{\Gamma^2 + (-\Gamma - \Delta q_0(t))^2} \tag{2.17}$$

Reworking this gives $\Delta q_0(t)$ as the peak-shift value:

$$\Delta q_0(t) \approx \Gamma \cdot \frac{1 - K(t)}{1 + K(t)} \tag{2.18}$$

The ratio-function $K(t)$ is simply determined experimentally.

$$I(t, q = q_{low}, q_0(t)) = \frac{a(t) \cdot \Gamma^2}{\Gamma^2 + (-\Delta q_0(t) - \Gamma)^2} \simeq I_0(g_{low}(t) + 1) \tag{2.19}$$

The function $\Delta q_0(t)$ can now be used as the last unknown in the expression for the intensity at either side of the peak:

$$I(t, q = q_{low}, q_0(t)) = \frac{a(t) \cdot \Gamma^2}{\Gamma^2 + (-\Delta q_0(t) - \Gamma)^2} \simeq I_0(g_{low}(t) + 1) \tag{2.20}$$

From this expression one can finally get the $a(t)$, the q-shift indepent intensity dependence:

$$a(t) \sim I_0(g_{low}(t) + 1) \cdot \frac{\Gamma^2 + (-\Delta q_0(t) - \Gamma)^2}{\Gamma^2} \tag{2.21}$$

Fluence dependence

A fluence dependence of the demagnetization behaviour at 105K is made. At 105K the demagnetization and recovery can both be conveniently captured within the 20ns time-window. The peak shift $\Delta q(t)$ is plotted as well as the shift-independent peak intensity. Time constants are again obtained with the fit function 2.13. From the fluence dependence it seems that there are two different regimes which can be accessed upon laser excitation. This can be easily seen by eye in the graphs, but it also becomes clear from the time constants.

The maximum change in the central position of the diffraction peak is $\Delta q_{0,max} \simeq 4{,}75 \cdot 10^{-3} \mathring{A}^{-1}$. According to the graph of $q_0(T)$ from the static measurement section (fits presented in 2.3.2 in the Appendix) this corresponds to an equivalent temperature change of $\simeq$ 4,5K. The peak position in ($\Delta q_0(t)$,I(t))-space is plotted in figure 2.14.

Above an excitation ratio of $\beta \sim 2{,}0\%$ of the free electrons, the interaction possibly starts to become nonlinear, as can be seen from the time constants.

Carrier excitation The amount of created carriers by the laser pulse can be calculated according to the relation:

$$N = \frac{(1 - R)F\alpha}{\hbar\omega} \tag{2.22}$$

Here $\hbar\omega$=1,5eV is the used excitation energy. R=0,352 is the reflection coefficient and α=2,75·10^5 cm^{-1} is the absorption coefficient for dysprosium at the used wavelength. F= f mJ/cm^2 is the

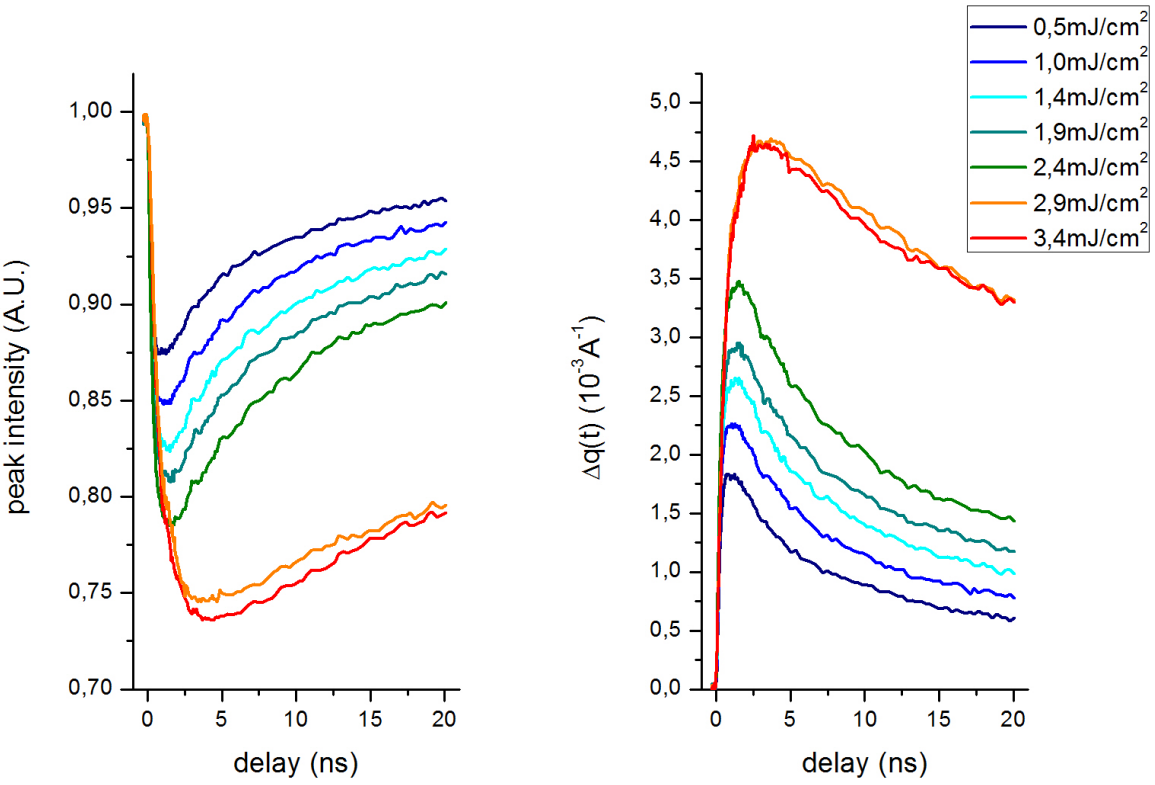

Figure 2.11: Relative diffraction peak amplitudes in time versus fluence. The right graph shows the peak shifts $\Delta q_0(t)$ in time versus fluence. The graphs are obtained according to the peak shift model presented in section 2.2.4.

used fluence. The number of atomic sites per cubic centimetre dysprosium can be calculated as $\sim$3,165$\cdot 10^{22}$. Elemental dysprosium is a metal with Dy^{3+} sites and such has 3 free electrons per atomic site. The percentage of the number of excited carriers N_{exc} per cubic centimetre to the number of free electrons per cubic centimetre is now given as: $\beta = 100\% \cdot N_{exc} / N_{valence} = f \cdot 0{,}781\%$. The carrier excitation ratio is indicated in the upper x-axis in graph 2.15.

RKKY-interaction The maxima in dI/I versus fluence have been plotted in figure 2.23 in the appendix. The dI/I increase linearly with increasing fluence. This is qualitatively in accordance with the fact that analytically the RKKY-interaction J has a linear dependence on the number of electrons $N(\epsilon_F)$ at the Fermi level: $J \sim N(\epsilon_F)$ [14].

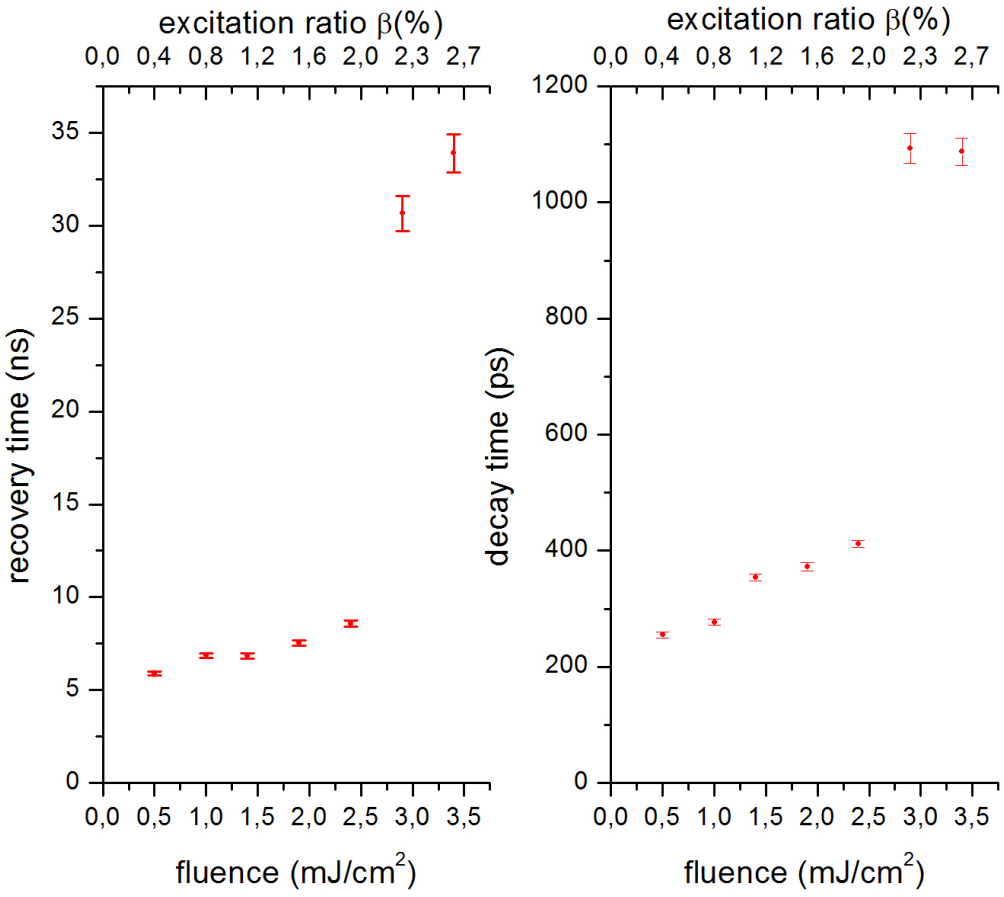

Figure 2.12: Time constants of the decay and recovery of the magnetic signal versus fluence. The time constants are obtained by fitting the intensity traces obtained with the peak shift model with the function 2.13.

Temperature dependence revisited

The temperature dependence of ultrafast perturbation of the antiferromagnetic order was again analysed, but now accordingly to the fit model presented above. The temperature dependent fit parameters are presented below. The time dependent temperature dependence graphs are presented in the appendix. The fits obtained according to the peak shift model show a different dependence on the demagnetization with varying temperature than the simple fit in section 2.2.4. If one does not take into account the measurement values at 150K and 160K it seems that the decay time starts to grow with increasing temperature and saturates around a value of 400ps. In the appendix normalized temperature traces are presented. The trace normalized to the minima qualitatively shows that the recovery time increases with increasing temperature. From the traces normalized to the value at 20ns there is no obvious trend visible.

Asymmetry of diffraction peak

The time dependent $\theta/2\theta$ scan presented in plot 2.9 shows a clear asymmetry in the peak. To investigate the origin of this asymmetry time traces on- and off-resonance were made and compared. The on-resonant trace is the usual trace as always presented where the on-resonance conditions are fulfilled with an x-ray energy of E=1338eV. The off-resonant trace was taken at the same 2θ position at E=1250eV. At this incoming x-ray energy the resonant term in the form factor 2.5 is negligible, plus the diffraction conditions are not fulfilled anymore since λ has changed. The

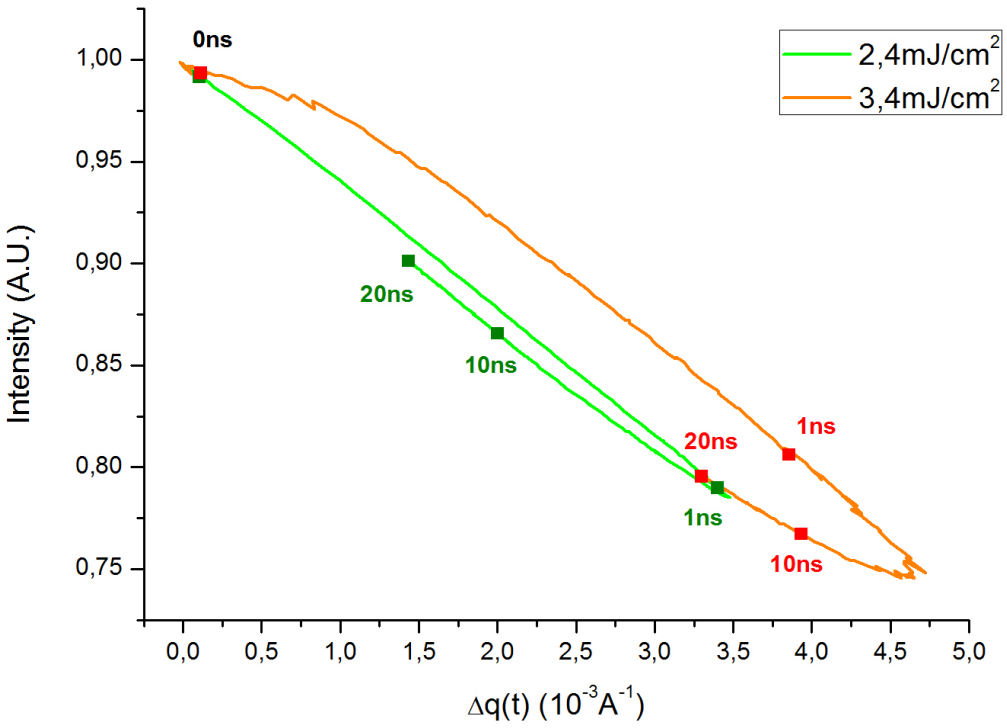

Figure 2.13: Position and amplitude of peak in time upon laser excitation ($\Delta q_0(t)$,I(t)). The trajectory is clockwise (the times at 0ns,1ns,10ns and 20ns are indicated). Two different demagnetization regimes depending on the used fluence show up.

x-ray reflectivity under the angle θ is now essentially measured. This forms a background signal to the diffraction scans. Also the background (multiplied by a factor 3333) shows a pump probe contribution.

A decrease in the x-ray reflectivity agrees with the scenario that the metallicity of the system decreases. This scenario is the case in Dysprosium, since upon laser excitation electrons are taken away at the Fermi level. This will decrease the "metallicity", hence the reflection coefficient.

Validity of the peak shift model

Graph 2.9 shows the diffraction peak in the ground state and the diffraction peak at t=1ns after perturbation for the T=105K measurement. The change at t=1ns at q_0 can be easily estimated as dI/I∼0,094. The peak shift model gives a change dI/I∼0,36, which is a big overestimation. This can possibly be due to the fact that in the peak model one assumes that the peak is a Lorentzian, while from the measurement in graph 2.9 it is clear that there is a rising background. The results can likely be improved by subtracting a straight line from the data or incorporate this in the model. When the intensity change at two additional q-values can be made (making a total of four) the slope (and possibly change in slope) can be taken into account.

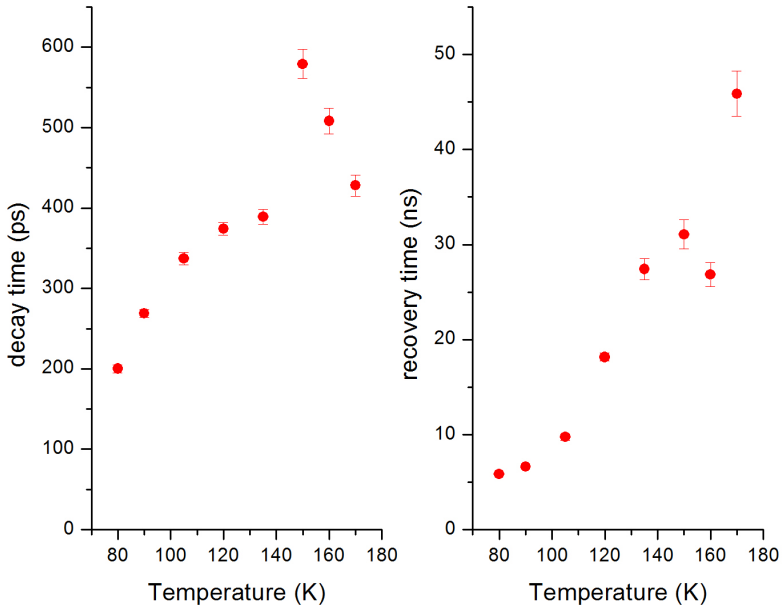

Figure 2.14: Temperature dependence of the time constants for the decay and recovery obtained according to the peak shift model.

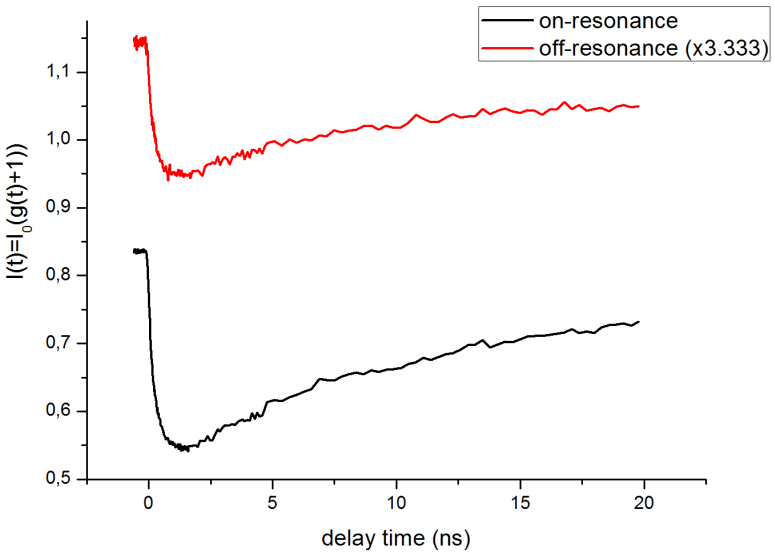

Figure 2.15: The black graph gives a time trace of the diffraction peak amplitude. This is when the resonance condition is fulfilled. The red graph gives a time trace whe the resonance conditions are *not* fulfilled. This background signal possibly is the time-dependent x-ray reflectivity of the Dysprosium. The decrease in reflectivity can correspond to a decrease in metallicity of the system.

Discussion

Previous work on ultrafast demagnetization Over the past 20 years a lot of effort has been put into understanding the mechanism behind ultrafast demagnetization [1]. A drop in magne-

tization means that the angular momentum of the spin system should flow into another angular momentum reservoir to fulfill conservation of angular momentum.

One can think that the spin momentum S flows into the orbital reservoir L of an atom. It was proven in nickel thin films by tr-XMCD that this is possible mechanism actually does not occur, i.e. the orbital momentum L does not act as a reservoir for spin momentum [15]. The implication of this experiment is that only the lattice is a viable reservoir to transfer the spin momentum to. The most likely microscopic mechanism for this is the Elliot-Yaphet spin-flip scattering. Here the laser pulse initially creates hot electrons. This excess energy is used to facilitate a spin-flip process where angular momentum is expulsed in the form of a phonon. Experimental findings in support of this model come from measurements which compare the ultrafast demagnetization in metallic systems like Ni and Fe which have a spin up and spin down band with half metals like CrO_2 which only has one spin polarization. In half metals the demagnetization times are long because there is not an opposite spin channel available for spin-flip scattering [16].

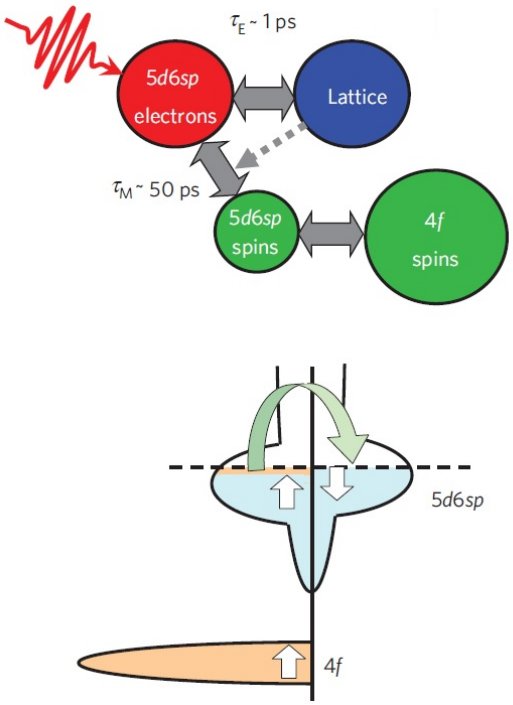

Figure 2.16: The pathways over which excess energy will dissipate into the lattice plus the angular momentum flow as described in [1].

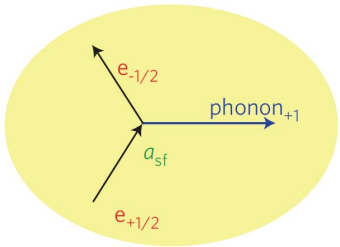

Figure 2.17: The Elliot-Yaphet mechanism. Excess energy can facilitate a spin-flip process which creates a phonon. Figure taken from [1].

The rare earth metal systems have an additional complication to the demagnetization problem due to the presence of multiple spin systems, i.e. the 4f-system and the 6s-system. The 4f and 6s moments are strongly coupled to each other by the RKKY-interaction. The first step in the ultrafast demagnetization is again the creation of hot electrons. Now there are two pathways how this additional energy can be used to transfer spin angular momentum away from the 4f electrons. The first one is an indirect process which extends the process described above for Nickel. Via the Elliot-Yaphet mechanism there is a spin-flip of the 6s electrons which creates phonons. In this way the lattice temperature increases. The 4f orbitals now see a changing crystal field. The 4f spin angular momentum now follows this changing crystal field via LS coupling. Support of this demagnetization scheme was given by comparing the demagnetization of Gd and Tb in a tr-XMCD study [17] Gd with orbital quantum number L=0 has a small spin-lattice coupling via LS-coupling while Tb has a strong spin-lattice coupling by L=3. It was found that the demagnetization time in Gd is 40ps, while in the stronger LS coupled material Tb this is 8ps.

The second one is a process where simultaneous demagnetization of the itinerant 6s moments and the localized 4f moments happen due to the strong coupling between the system: the 6s electrons make a spin-flip and the 4f moments follow by the RKKY-interaction. The spin angular momentum now dissipates into the lattice.

The above explanations of angular momentum dissipation are all possible for a ferromagnetic system. Antiferromagnets even open up an additional demagnetization pathway. Angular momentum from the -S magnetic sublattice can flow into the +S magnetic sublattice and vice versa. In this way angular momentum is also conserved.

This work The demagnetization constants generally fall within a time window of 100-600ps depending on temperature and used fluence in this dysprosium study. In the discussion on Tb and Gd in [17] the strength of the LS coupling comes forward as an argument to explain the differences in demagnetization times. For Dy the LS coupling will be even stronger (Dy, L=5). So according to this argument the demagnetization times of Dysprosium should be expected to be faster than 4ps. This is evidentely not the case in these measurements. In principle the same interaction is studied in both studies (RKKY), but there is a difference in the magnetic ordering (ferromagnetic versus helical antiferromagnetism in Dy). The ferro-component versus the antiferro-component in the RKKY-interaction could possibly be of an influence to the demagnetization times. As we measure long demagnetization times, a thermal origin of the demagnetization is plausible. Hot 6s-electrons are created, which lose their energy via Elliot-Yaphet scattering. As phonons are created, the lattice temperature increases. The 4f-electrons see a changing crystal field in this way, which gives rise to the demagnetization process.

The positive change in the $\Delta q_0(t)$ with an equivalent temperature change of 4,5K presented in section 2.2.4 can have different origins. One idea is that the excitation electronically changes the spiral winding. This is a dangerous statement looking to the equivalent temperature change. This small thermal change can likely just be thermal heating from the laser. Another viable option is that the positive $\Delta q_0(t)$ change is the result of lattice heating by the generation of phonons by the Elliot-Yaphet mechanism and the RKKY-exchange mediated dissipation of angular momentum from the 4f electrons into the lattice. The temperature change is very small. A likely explanation for this follows from the discrepancy between penetration depth of laser and x-rays. In this way the x-ray signal samples a non-perturbed part of the sample, hence giving a smaller change on average.

Element	L	τ_{decay}	Phase	Temperature	excitation	fluence
Gd	0	40 ± 10 ps	ferromagnetic	140K	1,5eV	3-5 mJ/cm^2
Tb	3	8 ± 3 ps	ferromagnetic	140K	1,5eV	3-5 mJ/cm^2
Dy	5	389 ± 9 ps	helical AFM	135K	1,5eV	1,4 mJ/cm^2

Table 2.2.4 gives an overview of the different demagnetization time constants in rare earth metals.

Interesting to note is that Koopmans et al. [1] mention two different fluence regimes leading to different behaviour in the demagnetization. This can possibly be seen in the fluence dependence of the demagnetization in Dysprosium, as shown in figure 2.13. They also work out a differential equation for demagnetization dynamics which should lead to better fits of the data. This equation is set up for the demagnetization of ferromagnets. A better option would be to set up a model with a bipartite lattice [18] for antiferromagnets.

Future work It would be interesting to perform tr- XMCD measurements to get information on the demagnetization time constants in Dysprosium in the ferromagnetic state. This would first of all give a fairer comparison with the work described in [17] than is now possible. Apart from that it would give full information on what is the role of the ferromagnetic component versus the antiferromagnetic component in the RKKY interaction in one material. The initial time dynamics upon laser excitation can be studied more thoroughly with a higher time resolution of $\simeq$ 100fs with the slicing technique [7].

2.2.5 Conclusion

The ultrafast demagnetization behaviour of the antiferromagnetic spiral in Dysprosium was studied by means of time resolved Resonant X-ray Diffraction. Upon laser excitation 6s conduction electrons at the Fermi are removed. This will decouple the RKKY exchange coupled 4f electrons in Dy, giving rise to a decrease in the magnetization, reflected as a drop in the diffraction intensity. The diffraction peak centre shifts to a higher q_0 position, which is an indication for the change in the spiral lenght. The origin of this shift could be an increased lattice temperature due to the generation of phonons. In order to account for the peak shift a fit model was made to deduce the time dependent shift and peak intensity drop. The decay times analyzed by this procedure fall in a range of $\sim$200ps at 80K to $\sim$600ps at 170K. The recovery times fall within a range of $\sim$5ns for 80K and up to $\sim$45ns for 170K. Two different fluence regimes could be distinguished in accordance with theory. The background x-ray reflectivity showed to have a pump-probe dependence. A possible origin of the measured decrease in reflectivity is the decrease in "metallicity" due to the removal of 6s conduction electrons at the Fermi level upon laser excitation.

2.3 Appendix

2.3.1 Experimental setup tr-RXRD experiment

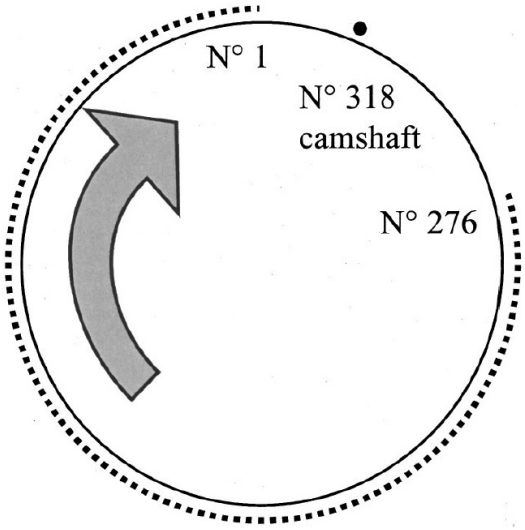

Figure 2.18: Top view from the synchrotron with an older type filling pattern with 1 camshaft. Taken from [8].

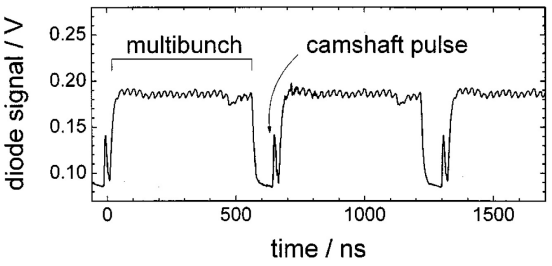

Figure 2.19: Corresponding X-ray intensity as detected on a photodiode and shown on a scope. Taken from [8].

Scattering chamber

The beamline endstation is a UHV scattering chamber. The top port is occupied by the motor which rotates a cryoarm. The sample can be placed on the cryoarm via a rod inside the sample load lock. A phosphorplate plus pinhole and a YAG crystal are mounted on the bottom part of the cryoarm for the alignment procedure. An avalance photodiode detects the x-ray signal. A photodiode which can see the laser and x-rays is used for alignment. A channeltron can be used to measure x-ray fluorescence. It is also possible to measure the x-ray drain current. The theta coordinate is the movement of the cryoarm. The 2theta movement gives a movement of the detectors. The APD is positioned +20deg away from PD which gives the detector position. The chamber calibrated in such a way that:

$$\theta_{diff} = (2\theta_{0,chamber} + 20^\circ - 2\theta_{chamber})/2 = (311.15^\circ + 20^\circ - 2\theta_{chamber})/2 \tag{2.23}$$

Setup of measurement

Finding the centre of rotation The sample is brought into the scattering chamber via the load lock arm. With the arm the sample is positioned inside the sample holder in the cryostat. The sample is cooled down to the desired temperature. This is done in order to outrule any possible drift in the alignment due to thermal contraction of the cryostat and sample later on. A camera is placed on the bottom of the chamber to view the cryoarm. By tracking the position of the YAG crystal on the cryostat after a 180° rotation and finding the common line, the centre of rotation (for the $\theta/2\theta$ move) can be determined. The centre of rotation needs to be indicated on the television screen. The YAG crystal should now be moved to the centre of rotation (COR). The COR should be indicated on the television screen. Now the chamber needs to be physically moved in such a way that the x-ray beam hits the centre of the YAG crystal/centre of rotation. In this way the COR of the $\theta/2\theta$ move lies in the incoming x-ray beam. Write down the (x,y) coordinates of the YAG crystal when it is positioned on the COR. The sample should now be put into the COR.

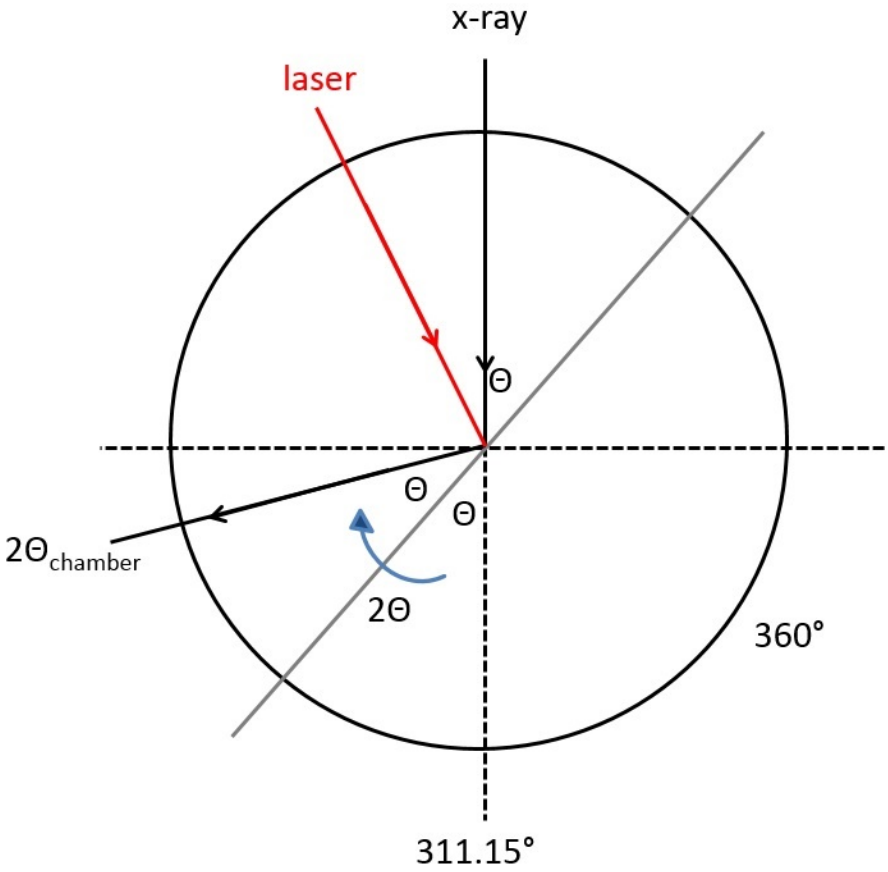

Figure 2.20: Schematics of the scattering chamber.

That this coordinate is really on the sample can be checked by measuring the absorption edge via the sample current. Also save the (x,y)-coordinates of the sample-COR position. The θ-coordinate of the direct x-ray beam can be found by looking for the x-ray signal on the photodiode and the avalanche photodiode. Both coordinates should be saved for later reference.

Spatial overlap of pump laser and x-ray beam The pump-laser enters the chamber via a viewport under a $\approx 15°$ angle with respect to the x-ray beam. To start with the spatial overlap of the x-ray and laser the pinhole (which is positioned at the same depth as the YAG) is moved to the COR. Scan the z-direction of the pinhole and see on the detector where the x-ray passes through the pinhole. Store this z-coordinate. Now manually aim the alignment laser through the pinhole and maximize the signal by looking to the transmission signal on the photodiode.

Determination of beam size The beamsize of the x-ray and the laser can be measured in the following manner. Place the detector behind the knife-edge. Now do a z-scan, look to the laser signal on the photodiode and fit the profile with a error function. The FWHM gives the beam size in the z-direction. The same thing can be done for the x-width of the beam. Repeat this for the x-ray beam size. The beam size of the laser can be adjusted by moving the focusing mirror. The beam size of the x-ray can be altered by moving the M203 bending mirror.

Maximizing scattering intensity First of all one should make sure that the x-ray probes the sample. This is done by doing an x-ray absorption edge scan via the sample current channel (or fluorescence yield via the channeltron). Now the resonant diffraction peak needs to be located. If the peak is located the best undulator gap for the specific energy should be determined. When the

undulator gap is moved (the distance between the undulator magnet arrays) the output spectrum I(λ) changes. Now do this EPU gap scan on the peak and see where the intensity I(λ, edge) is maximum. Use this undulator gap setting for the experiment.

Relative position of the θ-arm and 2θ-arm In order to make proper rocking curves ($\theta/2\theta$ scans) the sample holder angle or θ angle and the 2θ or detector angle should be properly calibrated to each other. This is done by first roughly finding the peak. Then perform a peak scan by scanning θ with fixed 2θ angle. Go to the θ with maximum intensity. This corresponds to maximizing the Bragg condition. Set this θ . Now do a 2θ scan and find maximum intensity. Set the 2θ motor to this 2θ angle. This is done to ensure that proper rocking curves are made. The 2θ should be covered since we work with a small detector with a small angular width. In case one uses a big CCD detector it suffices to only optimize the Bragg condition by scanning θ.

Trajectory scan A sample specific so-called trajectory scan should be done to further maximize the diffraction signal. In the trajectory scan the x-ray energy is scanned around the absorption edge energy in order to enhance the scattering intensity. Since the x-ray energy now changes during this scan the incoming wavelength also changes. This will also alter the diffraction conditions and angles. In order to account for this, a table with energy, corresponding $\theta/2\theta$ angles and lattice parameters is uploaded. The energy where the diffraction peak is maximized should be used for the experiment.

Timing initialization Different trigger signals from the storage ring and the x-ray chopper (located at the upstream chamber) are brought to a central timing unit called the FPGA. The out 6.02 encoder signal gives a trigger pulse from the x-ray chopper to the FPGA with the chopper revolution frequency. This signal is first delayed with a fixed time delay A before it enters the FPGA. Since the chopper always runs by itself, this delay basically makes that the probed part of the complete synchtrotron ring is moved. The out 6.02 index signal indicates which chopper slot is open. Not every chopper slot is equally spaced, so different chopper slots have slightly different time delays. This signal is necessary to later correct the timing in the FPGA program.

Other signals which go into the FPGA are the ring frequency ($\simeq$ 500MHz, bucket-to-bucket freq) and the Storage Ring Orbit Clock (500MHz/328 buckets $\simeq$ 1,523MHz). The latter one indicates in which bucket the camshaft is located.

The entire diffraction signal (non-gated boxcar signal i.e. bypassing the boxcar) can be put on a scope. In the correct time window (t 600ns) one chopper slot is shown. Now the boxcar window (adjustable time window, set it at 2ns to gate the camshaft) should be moved over the camshaft signal by moving time delay B. The use of the boxcar is to only sample the x-ray signal from the camshaft. The x-ray signal from the multibunch also enters the boxcar, but this is gated away in the output signal of the boxcar. In this way a higher signal-to-noise ratio is acquired than without the boxcart.

The laser system is also triggered by the FPGA. This laser system consists of a pump laser, a Ti:Sapphire oscillator and a regenerative amplifier. Inside the laser optics system a tiny part of the beam is drained away into a laser diode, which gives a trigger signal. This trigger signal can then be used on the scope as a reference of where the laser comes in at the sample in time relative to the chopper window background. Now shift the laser system by delay box B to a camshaft in the center of the chopper window. In this way a rough timing initialization is gained. The real time zero is found by doing a electronic time scan on a diffraction peak. Here now only the laser system moves relatively to the camshaft. The time where the peak drops is the t_0.

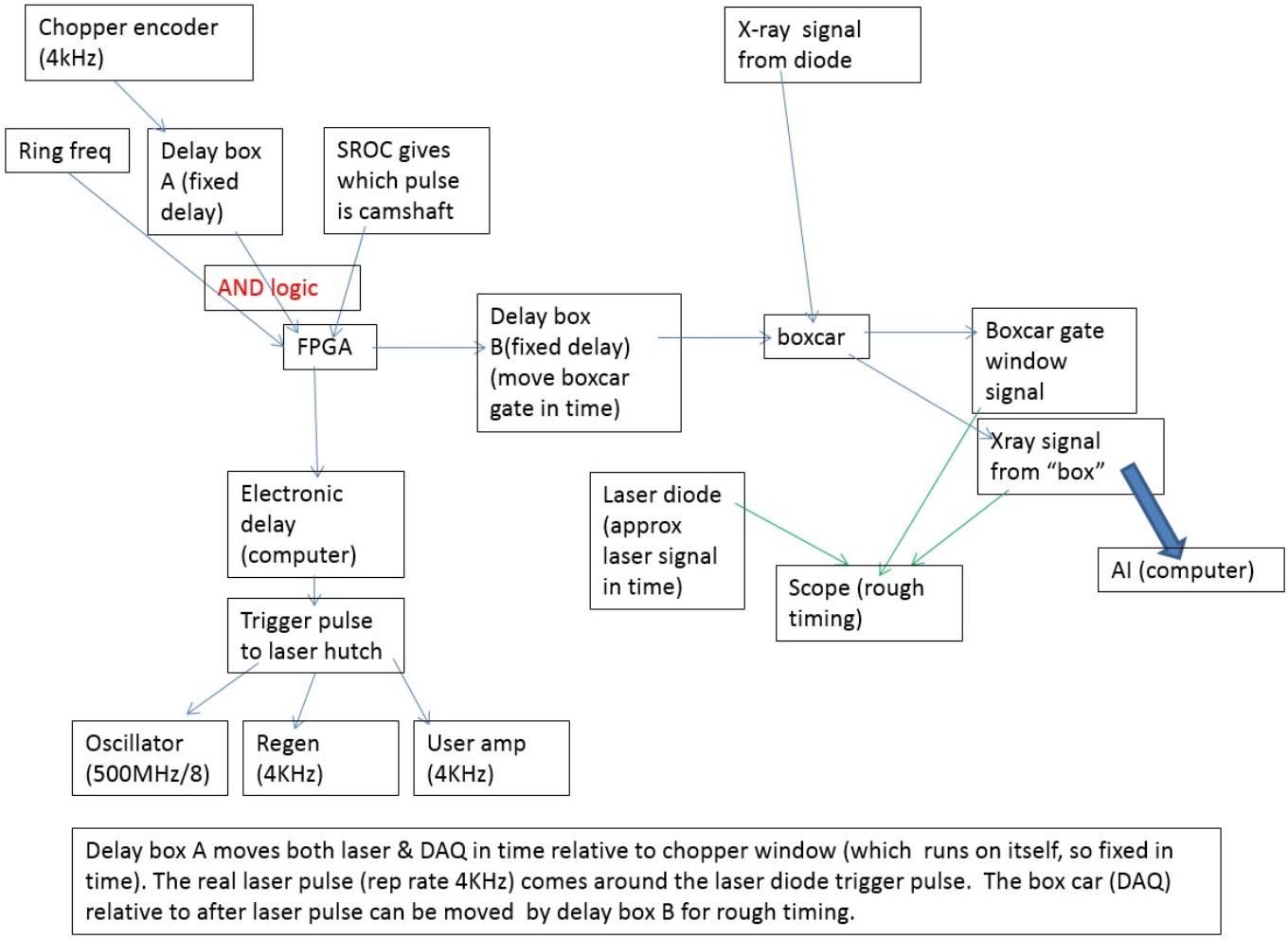

Figure 2.21: Overview of the data-acquisition scheme and triggering sequence.

Acquiring different time spans

Recovery times of diffraction peaks can vary from nanoseconds to minutes depending on laser fluence, temperature, laser wavelength, etcetera. It is therefore important to have the flexibility to follow peak recovery in different time windows. One should also take into account the laser repetition rate versus recovery times. If one acquires data with a 1KHz rep rate of the laser the recovery time should at least be smaller than a millisecond, else the sample will be double pumped. Below here the different time windows and their respective methods are summarized.

The pulse size from the laser oscillator is around 100fs and with a repetition rate of 67MHz the pulse separation is around 16ns. The regen amplifier and the user amplifier both have temporal gates in which they amplify the incoming pulses of the oscillator. These temporal gates are the Pockels cells time windows.The phase of the oscillator can be shifted by a so-called Dazzler (acousto-optic programmable dispersive filter). In this way the pulse is temporally shifted within a Pockels cell time window. In this way the following windows can be accessed (step size/window size): 10ps/1ns and 100ps/10ns. The phase shift of the Dazzler is the electronic time delay.

If now the Regen/User Pockels cell time windows are moved from oscillator pulse to oscillator pulse the step size will be in the order of $\simeq$16ns. This gives time windows of 1ns/100ns and 10ns/1000ns

The 100μs window gives a priori a slight technical problem. The chopper window has a temporal width of around 10μs. This is smaller than the 100μs you want to cover. From the data acquisition scheme we see that the chopper gives a trigger signal to the FPGA, which in turn triggers the laser. So intrinsically the laser is always triggered after the chopper, which makes it of course impossible to let the laser come in before the chopper window. To solve this problem the data acquisition delay (delay B) is moved by a fixed delay of $\Delta t \simeq 250\mu$s. The laser pulse arrives in the first chopper window while the gated camshaft is located in the second chopper window. Since there is jitter in the chopper windows (not every chopper window has the same time delay) you should wary a little. In this way the laser pulse is triggered at different times with respect to chopper window two. Luckily this jitter is only maximally 1 chopper window big, so around 656ns $\simeq 1\mu$s. In this way the total jitter will be 1μs on a 100μs scan range. From here on it also starts to get useful to lower the repetition rate of the laser.

The range for 1s/minutes is fairly easy to accomplish. Put the laser on the lowest possible repetition rate, start measuring the x-ray signal and now quickly open and close the laser lock. In this way only one laser pulse passes through.

2.3.2 Results

Static temperature dependence

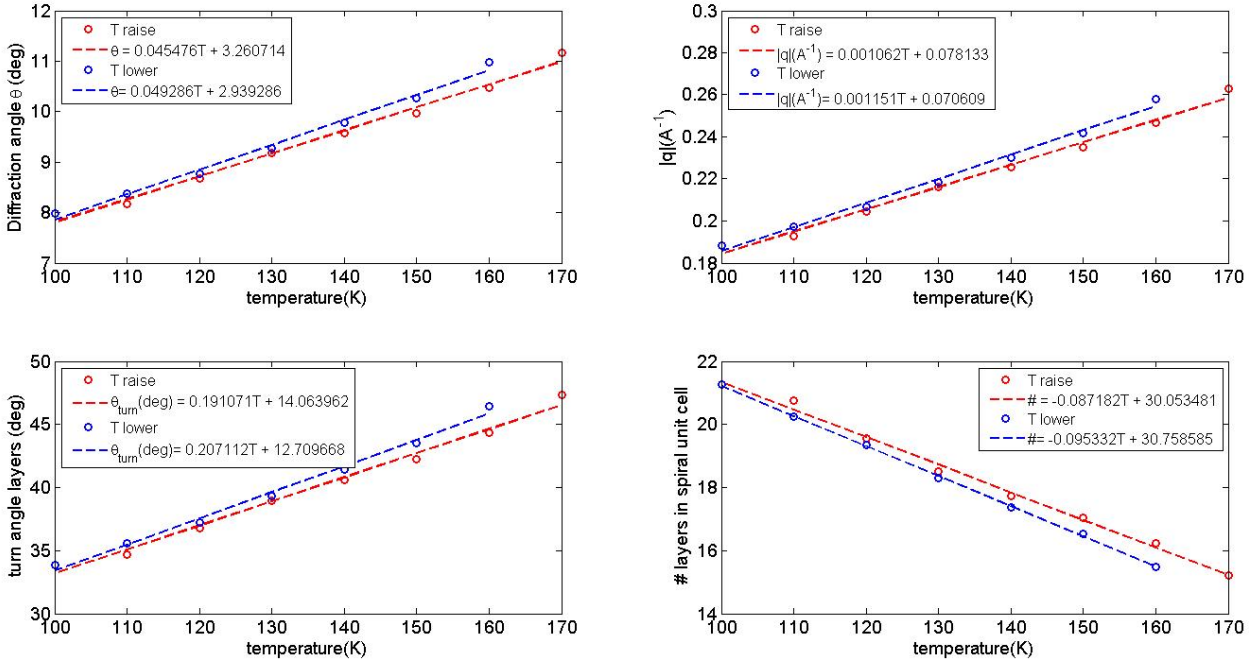

Figure 2.22: Schematics of the scattering chamber.

Fluence dependence

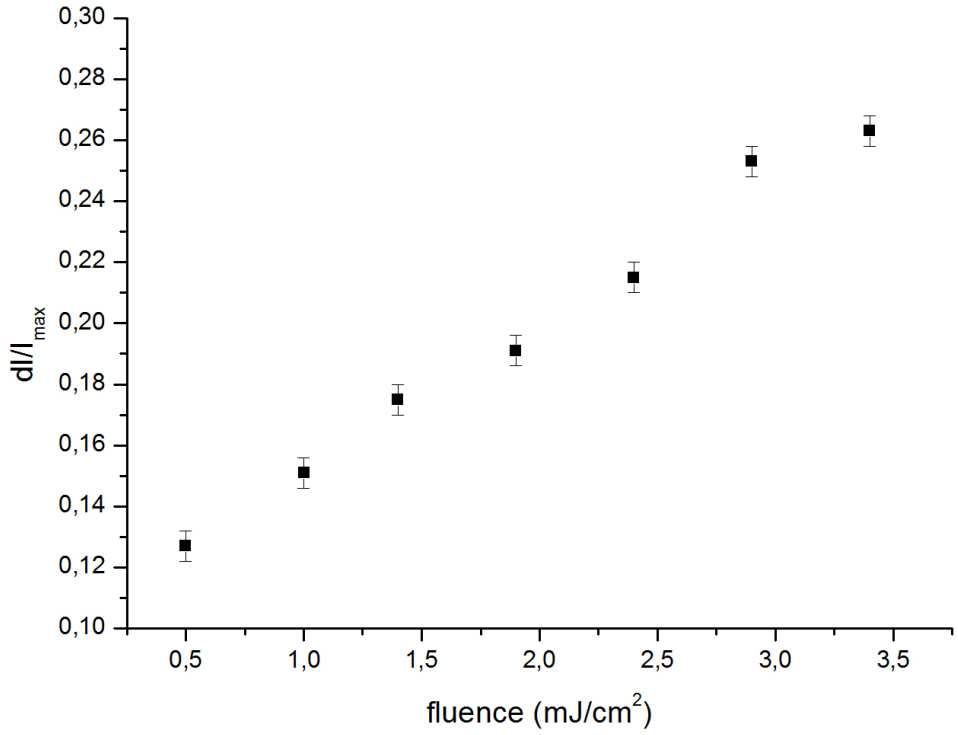

Figure 2.23: dI/I maxima in the fluence dependence.

Dynamic temperature dependence

Graph 2.25 gives all demagnetization curves obtained according to the peak shift model.

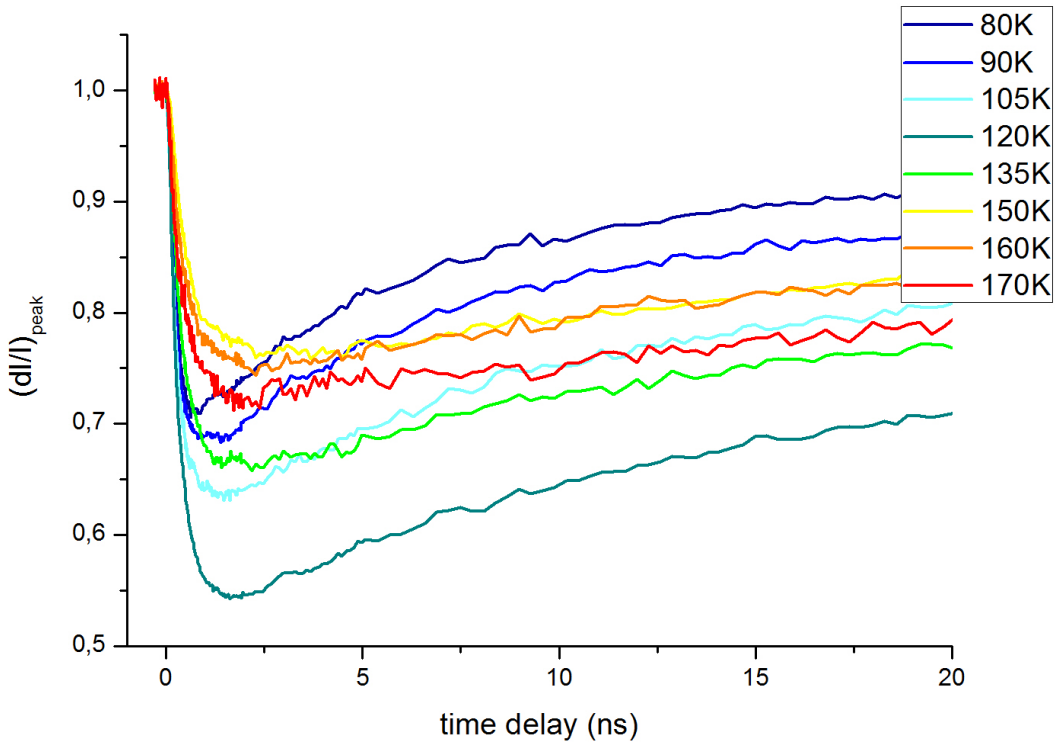

Figure 2.24: All temperature dependent demagnetization curves obtained according to the peak shift model.

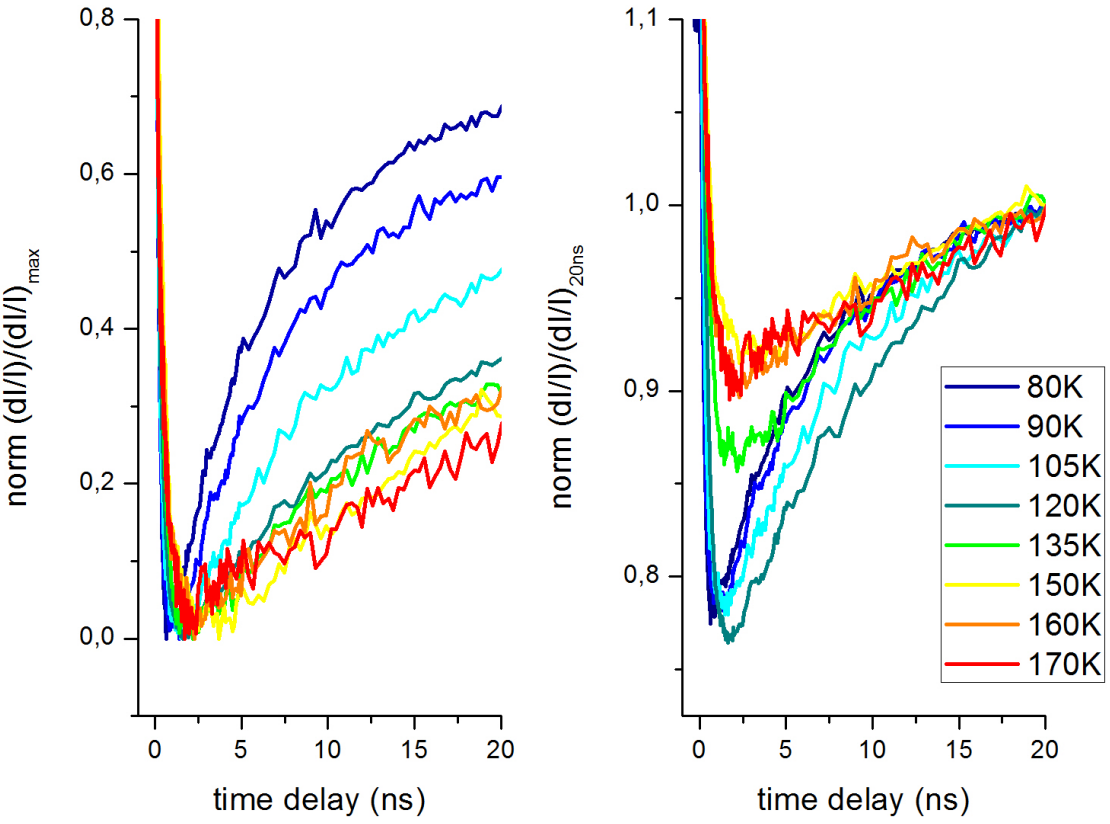

Figure 2.25: The left graph shows the temperature dependent demagnetization curves normalized to their respective minima. The right graph shows the curves normalized to their respective values at 20ns.

Chapter 3

Carrier dynamics in the 3D topological insulator Bi_2Se_3

3.1 Topological insulators

Topological insulators are insulating materials with gapless states at the surface. These states are formed by topological effects that make electrons travelling at the surface insensitive to scattering by nonmagnetic impurities. Topological insulators very likely provide new pathways for generating exotic condensed matter phases [19] and will very likely be beneficial to technological applications such as spintronics and quantum computing [20].

Topological surface states Topological surface states are found in materials which have a high atomic mass number, - giving rise to a high spin-orbital coupling -, and a small bandgap. The strong spin-orbit coupling makes that a spin-orbit split band (a band necessarily originating from atomic levels with orbital quantum number $l \neq 0$) can have an energy lowering $\Delta H = \lambda \langle \mathbf{L} \cdot \mathbf{S} \rangle$ and ends up below a band originating from atomic levels with orbital quantum number $l - 1$. The high atomic mass is beneficial to the energy change ΔH as $\lambda \sim Z^4$ where Z is the atomic number. A practical example is that for the semiconductor Bi_2Se_3 where the band originating in 6p-states ends up having a lower energy than the band originating in the 6s-states owing to the $\Delta H = \lambda \langle \mathbf{L} \cdot \mathbf{S} \rangle$ term. The "vacuum" surrounding the crystal has a s-p parity ordering of the energy levels (considering the vacuum an "insulator" with a 511MeV band gap), while now the crystal has the parity of the energy levels reversed as p-s. In order to have a continuous transition of the p-s parity ordering in the bulk to the s-p ordering of the vacuum, surface states will appear.

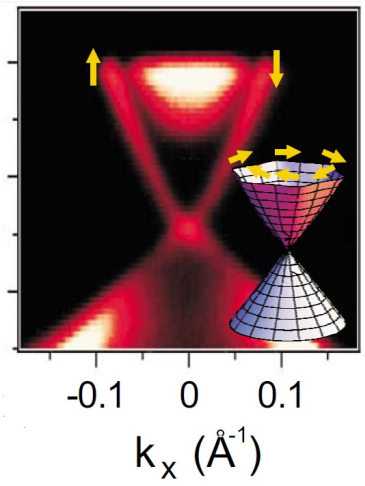

Figure 3.1: ARPES image from Bi_2Se_3 along the k_x direction in momentum space. The surface state Dirac cone is visible, as well as the bulk conduction and valence band. Figure taken from [21].

The situation where surface states appear at the interface of two materials of different parity orderings is drawn in figure 3.2. For the two-dimensional situation where a topologically nontrivial insulating layer is sandwiched between two trivial insulating layers, two edge states appear. For the 3D topological a Dirac cone appears, which is the Brillouin zone representation of the surface state. This Dirac cone and a cut-through in momentum space of the cone can be seen in figure 3.1.

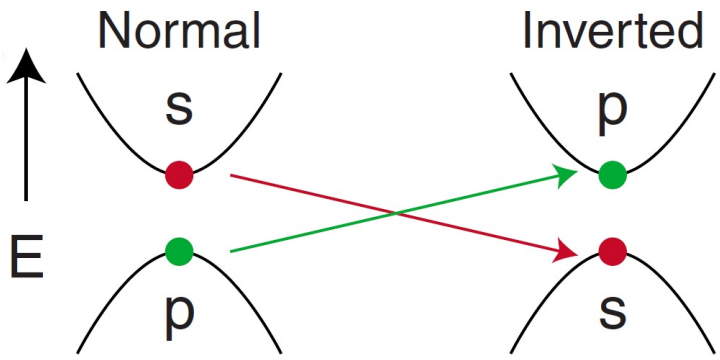

Figure 3.2: Owing to a high spin-orbit coupling the Hamiltonian term $\Delta H = \lambda \langle \mathbf{L} \cdot \mathbf{S} \rangle$ becomes big and a band inversion happens. When going from p-s parity ordering (nontrivial) to s-p (trivial) surface states appear. Figure taken from [21].

Bi_2Se_3 The topological insulator Bi_2Se_3 has a band gap of E_g ~0.3eV. The surface states are described by a single Dirac cone at the $\mathbf{k}$=0 Γ point of the Brillouin Zone. It has a rhombohedral crystal structure with the space group $D^5_{3d}(R\bar{3}m)$. The crystal unit cell consists of five atoms and can be seen in figure 3.3. One can see that Bi_2Se_3 has a layered structure. The unit cell consists of five layers. The full unit cell length is also referred to as a "quintuple layer". The Dirac cone in Bi_2Se_3 is seen in 3.1.

Spin-momentum locking The surface state in topological insulators is robust against nonmagnetic impurities and surface disorder. The forward and backward moving topological surface states are a pair of time-reversal conjugate states, i.e. under the time-reversal symmetry operator $\hat{T}$ the state $|\uparrow, k\rangle$ changes to $\hat{T}|\uparrow, k\rangle = |\downarrow, -k\rangle$ with the opposite spin orientation. In this way an electron cannot scatter into the opposite channel without changing its spin orientation. Hence the surface state is robust against nonmagnetic impurities (which do not have a finite angular momentum component to pick up). In this way the scattering from channel $+k$ to $-k$ is suppressed. The coupling between spin and the momentum is referred to as *spin-momentum locking* [23].

Relation to thermoelectricity 3D topological insulators also show to be excellent thermoelectric materials [23]. Thermoelectricity is the effect where a temperature gradient sets up an electric potential, which can be used for power generation. The performance of a thermoelectric material is expressed by a figure of merit ZT. For thermoelectricity this coefficient is:

$$ZT = \frac{S^2 \sigma}{\kappa} T \tag{3.1}$$

Here S is the Seebeck coefficient, σ the electrical conductivity and κ the thermal conductivity. A high Seebeck coefficient S asks for a low electrical conductivity. A high electrical conductivity gives a high thermal conductivity. In this way an optimum exists in these parameters. Topological insulators fulfull these properties. The low band gap E_g ensures that there is a relatively high

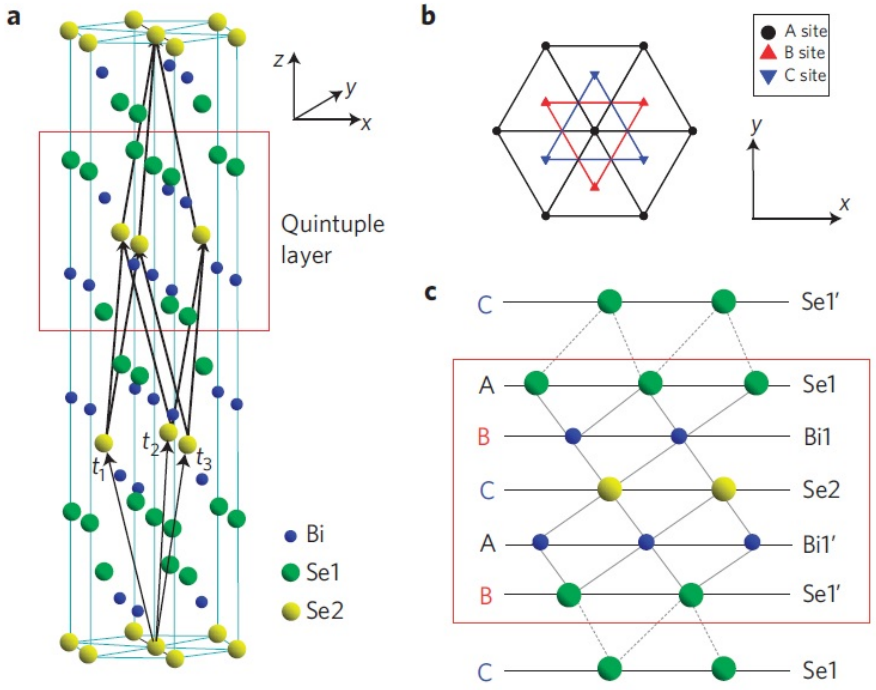

Figure 3.3: The Bi_2Se_3 unit cell. Figure taken from [22].

carrier concentration upon impurity doping. The high atomic mass elements of the topological insulators ensure a low thermal conductivity [23].

3.2 Surface state selective dynamics studies on Bi_2Se_3

Dynamic studies on 3D topological insulators ultimately beg for a method to obtain surface-state selectivity, i.e. it is wishful to rule out a bulk contribution. Two time-resolved studies which unequivocally probe surface state dynamics have been described in [24] and [25]. These studies will be shortly described to support and guide the motivation of our experiment.

3.2.1 Previous studies

Ultrafast ARPES

Study [25] described an ultrafast ARPES study in which a p-doped Bi_2Se_3 sample is used. The p-doping lowers the Fermi level to the Dirac-point. The time, energy and momentum resolution of the used setup allows to measure both bulk and surface contributions to the ARPES signal. A 1,5eV pump pulse populates high-lying bulk states, which rapidly decays to the bottom of the bulk conduction band (BCB). Within ∼2ps a hot Fermi distribution forms. This population reservoir fills the energetically lower surface states. The subsequent decay from the surface state is slower and persists for ∼10ps. Figure 3.4 shows the transient BCB, BVB (bulk valence band) and surface state occupations at various times after excitation.

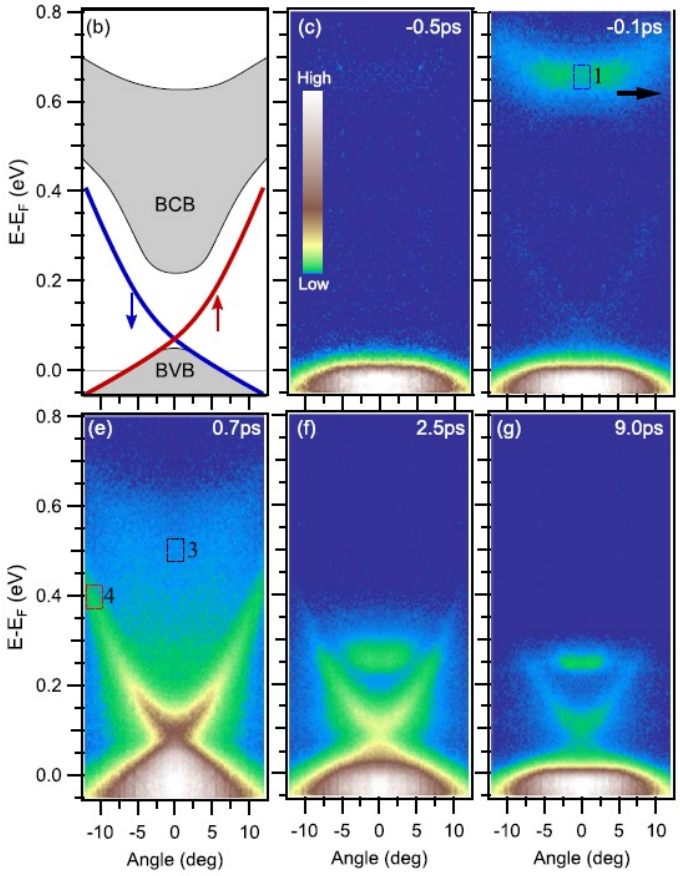

Figure 3.4: ARPES spectra at various time delays after a 1.5eV pump pulse. At pre-time-zero the surface states are unoccupied. At 0.7ps the surface states are populated with carriers which decay from the hot Fermi distribution in the bulk-conduction band. Figure taken from [25].

Second harmonic generation

Bi_2Se_3 has an inversion symmetric crystal structure. In the study [24] surface sensitivity is obtained by measuring the I(2ω) contribution to the reflection. For inversion symmetric crystals the second harmonic signal in the bulk is necessarily zero, except at the surface where the inversion symmetry is broken. Bulk carrier dynamics are distinguished by measuring the change in the reflected signal I(ω), originating from the first-order polarization. A relaxation time of ~1.2ps was measured. The differential signal is negative and an oscillatory component originating from an A_{1g} phonon can be seen. The bulk spin response is measured by applying circularly polarized pump pulses. This creates a non-equilibrium spin-polarized charge distribution. This transient spin-polarized charge distribution manifests itself as an effective transient magnetic field, which can be consequtively measured by the Kerr effect. A rapid decay of ~100fs is found for the bulk Kerr signal $\theta_K(\omega)$.

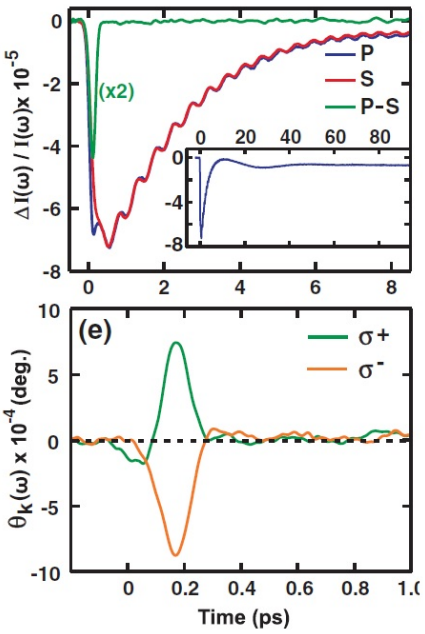

Figure 3.5: The upper graph shows the differential I(ω) trace. This gives the relaxation time τ ~2.3ps for the bulk charge carriers. s and p refer to the incident polarization with respect to the sample. Figure taken from [24].

The same can be done for the surface, looking to I(2ω). This shows a decay time of ~1.2ps for the relaxation of excited surface state carriers. The spin-decoherence time is determined as τ ~200fs.

3.2.2 Our study: spin dynamics by transient grating technique

It is envisaged to extend the already described carrier dynamics studies [26, 27] to the thin film variant, but more importantly measure diffusion properties with the transient grating setup. In a transient grating experiment two pump pulses excite the sample under a finite angle. This produces a spatial modulation of the optical properties by spatial carrier excitation. A third pulse can diffract from this spatial modulation in the refractive index. An equal number of electrons and holes is generated. Measuring the grating decay time for various grating periodicities allows to obtain the ambipolar diffusion coefficient (electrons carriers and hole carriers are created upon excitation) By plotting the inverse diffusion time constants versus the inverse grating period the ambipolar diffusion constant can be extracted.

Two parallel polarized pump beams create an intensity modulation on the sample as described above. Cross polarized pump beams create a uniform electric field, but the polarization is spatially modulated. A linear probe beam will also diffact from this grating. This experimental configuration allows to extract the spin diffusion coeffient.

We aim to measure the spin diffusion time in Bi_2Se_3, and specifically of the surface state. The process we envision to happen upon excitation with a spin grating is schematically shown in figure 3.6. At t=0 the pump pulses are applied, creating a spin-grating at the Fermi level. In this way a spin-polarized hole-grating is made (black) and a spin-polarized electron-grating. The electrons end up in the bulk conduction band. The spin-polarization in the bulk-conduction band is quickly lost (τ ~200fs), while the hole-grating in the surface state likely shows a longer decoherence and

diffusion process owing to spin-momentum locking. In this way the probe can scatter from a spin-polarized hole-grating.

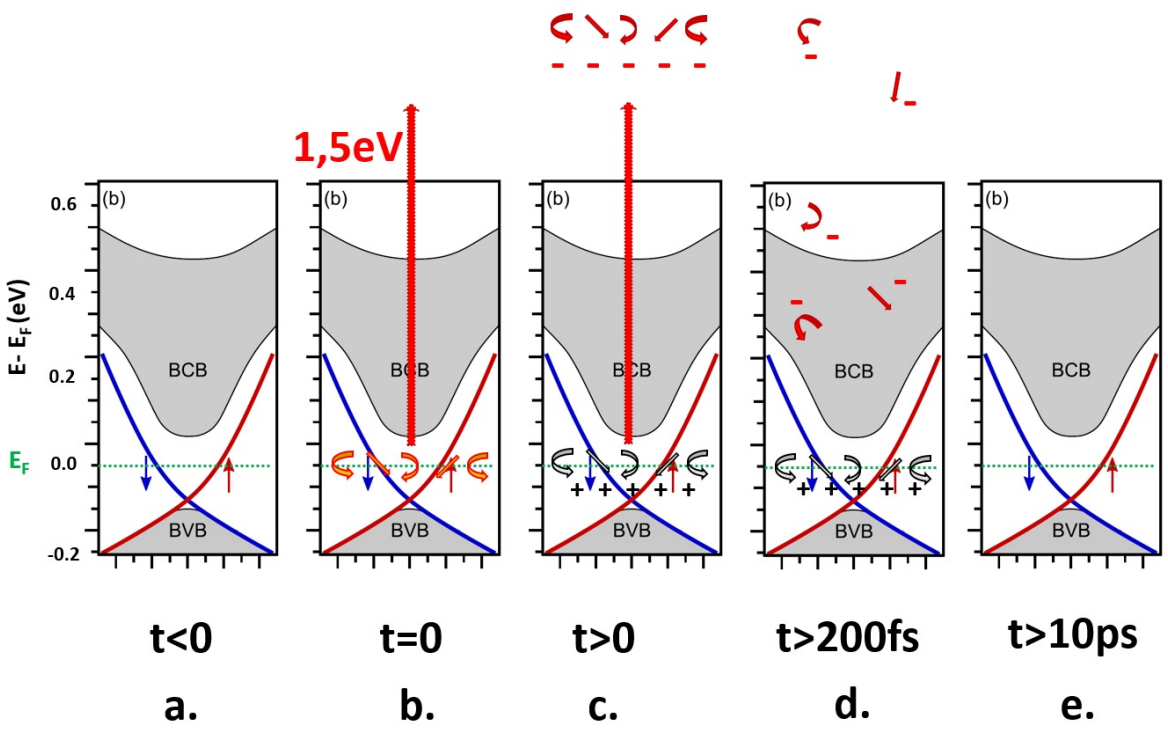

Figure 3.6: Idea what happens when a spin-grating is set up at the Fermi level. The 1,5eV laser pulse promotes the electrons to the bulk valence band. Spin coherence is rapidly lost in the BCB, while the hole-spin-grating remains in the surface state owing to spin-momentum locking. Figure adapted from [25].

3.3 Sample characteristics

The used sample for this study is a 20 Quintuple-Layer (20QL) thin film of Bi_2Se_3. The sample is grown by Molecular Beam Epitaxy on a c-axis oriented Al_2O_3 substrate in the group of S. Oh at Rutgers State University. We chose to work with thin film variants of Bi_2Se_3 as in these samples the presence of bulk carriers is greatly suppressed. It has been shown that in these 20QL-thick films the surface-to-bulk conductivity ratio is around σ_{SS}/σ_{BS} ~600 [28]. This systematic study shows that for our thin film has an areal carrier density of $n_{SS}=3\cdot10^{13}cm^{-2}$. The "areal" bulk contribution can be determined according to the relation n_{BS}=(film thickness[cm])$\cdot(1.6\cdot10^{18}cm^{-2})$. As 1QL≈1nm this gives a $n_{BS}=3.2\cdot10^{12}cm^{-2}$ for our 20QL film. In this way the surface-to-bulk carrier ratio is n_{SS}/n_{BS}~9.4, showing that surface electrons dominate over bulk electrons in our sample. The thickness dependence of the carrier concentration and conductivity from this study is presented in the appendix.

Below 10QL the Fermi level continously shifts away from the Dirac point [29]. Above 10QL the Dirac point - Fermi level separation stabilizes at 0.12eV, as can be seen in figure 3.8. An ARPES image where the Dirac point and the Fermi level are separated by 0.12eV is shown 3.8.

STM-images of our sample have been made in the group of Prof. Banerjee. One of these images is shown below in figure 3.7. From this image it can be seen that the Bi_2Se_3 thin film sample has terraces and that the amount of layers fluctuates.

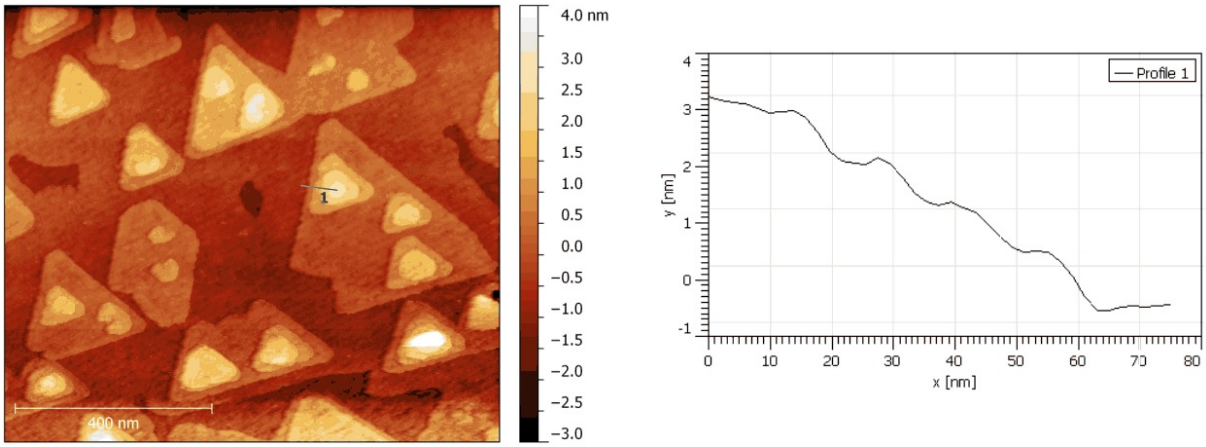

Figure 3.7: STM image of the thin film sample. The sample consists of a non-uniform surface which has a fluctuation of ±3 QL in height. Image courtesy of Prof. Banerjee.

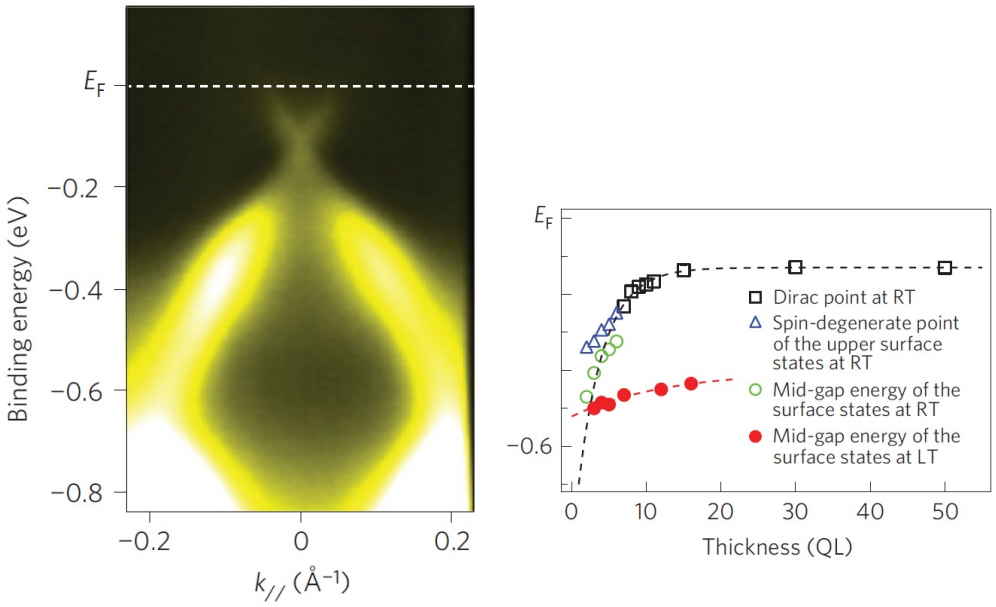

Figure 3.8: Bi_2Se_3 thin film characteristics. (a) ARPES image of 50QL Bi_2Se_3 . For this thickness the Dirac point lies 0.12eV away from the Fermi level as in our 20QL sample. (b) Location of the Dirac point. Above a thickness of 15QL the Fermi level - Dirac point separation remains 0.12eV. Figures taken from [29].

3.4 Ultrafast reflectivity study

3.4.1 Experimental setup

For the ultrafast reflectivity study a KML Ti:Sapphire cavity dumped laser (central wavelength λ=800nm) was constructed. Under normal operation the laser the laser produces a 80MHz output. The pump pulse fluence can go up to $8\mu J/cm^2$ at the sample position. When the laser is switched to the cavity dumped system it operates with a repetition rate of 808kHz and the maximum pump pulse fluence goes up to $40\mu J/cm^2$. The pulse length was determined by measuring the autocorrelation function of the pump and probe pulse in a BBO crystal. Considering the "smearing" of time-resolution due to the finite angle between pump and probe beam ($\theta \sim 9°$) the final time-resolution of the setup is $\tau \sim$ 33fs. This high value likely originates in the fact that the prism compensator in the setup was set to overcompensate.

The pump and probe polarizations are crossed in order to reduce pump scattering at the detectors. The pump is s-polarized and the probe p-polarized. As we work with a thin film we can measure both the change in reflection and transmission.

3.4.2 Results

Fluence dependence

A fluence dependence at T=293K was made. Low-fluence measurements were made with a 80MHz repetition rate. The fluence regime between 8-40$\mu J/cm^2$ is covered by the 808kHz repetition rate cavity dumped settings. The differential reflection signal graphs for the cavity dumped mode (808kHz rep. rate) are shown in the appendix in graph 3.21. The traces are fitted with a single exponential plus an ingrowing component which is convolved with a Gaussian. The Gaussian has a fixed $\sigma \sim$ 33fs, which corresponds to the pulse duration. The ingrowing and decay time constants versus fluence are presented in graph 3.9.

As can be seen from graph 3.9 the time constants in the 80MHz measurements have bigger error bars than the 808kHz measurements. This likely originates in the fact that the 80MHz data was taken with a "step scan" setting while the 808kHz data was taken with a "sweep scan" setting.

The decay times show to be on the same order of magnitude, but nevertheless ∼2x as fast as the data presented by Kumar et al. [26]. The sign of the measured reflectivity change agrees with the sign change described in [24]. The negative reflectivity change was also measured in the 1kHz regenerative amplifier set.

The ingrowing component can be resolved with our $\tau \sim$ 33fs resolution. The rise is caused by thermalization and energy relaxation of the created hot electrons. Our study shows that the thermalization and relaxation time decreases with increasing excited carrier concentration. This is in agreement with the measurements presented in [26].

Temperature dependence

The change in reflectivity and transmission upon laser excitation is monitored over a temperature span of 77K-290K. The traces (see appendix, graph 3.23) are again fitted with an ingrowing and decaying exponential convolved with a Gaussian. There is a discrepancy between the reflection and transmission decay times. This likely originates in the fact that the used fit function does not account for the presence of the acoustic phonon in the differential signal.

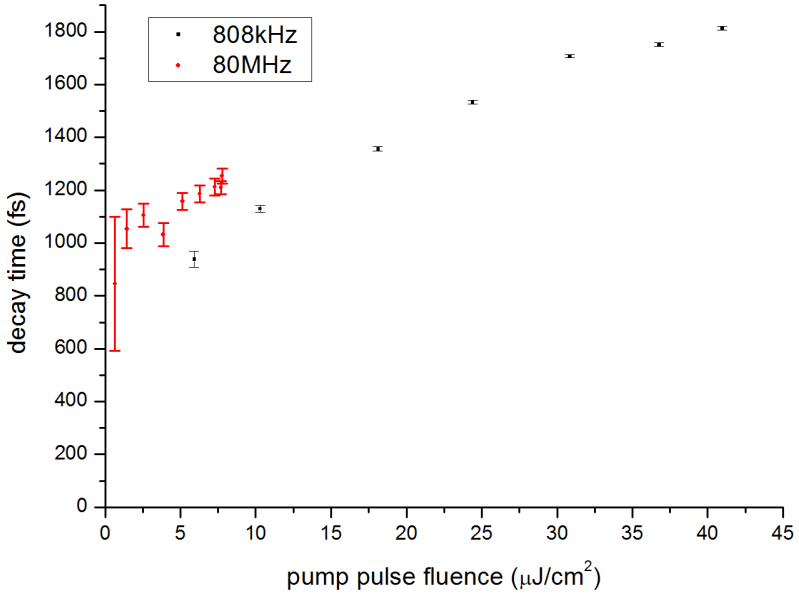

(a) Time constants for the decaying component.

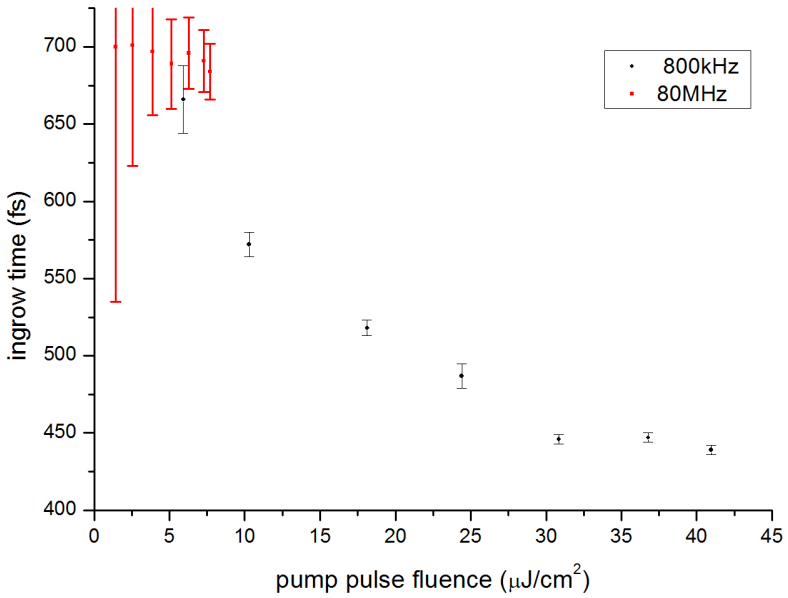

(b) Time constants for the ingrowing component.

Figure 3.9: Time constants for the fluence dependence.

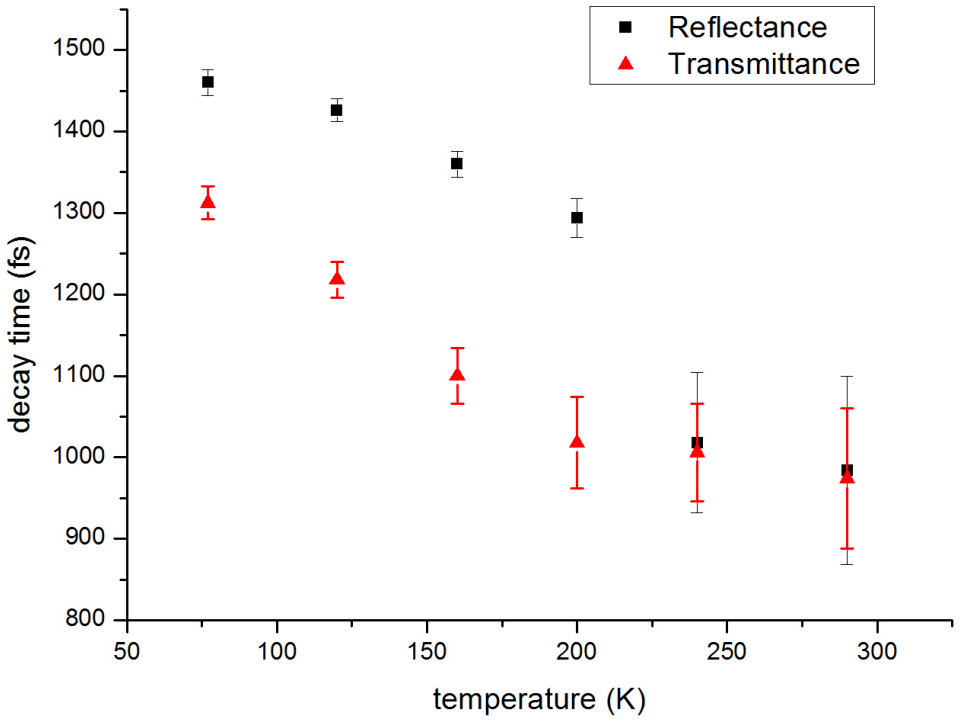

Figure 3.10: Decay time constants for reflection and transmission change. The decrease in time with increasing temperature is due to increasing phonon population with higher temperatures.

3.4.3 Discussion

Previous measurements Some ultrafast reflectivity studies have already been carried out on Bi_2Se_3 single crystals [26, 27]. In these studies a positive differential reflection signal is measured. The pump pulse is higher in energy than the band gap ($\hbar\omega$=1,5eV vs. $E_g \sim$ 0,3eV). Electrons from the valence band will be promoted to the conduction band. As now the conduction band states have a higher occupation number the absorption will decrease, giving an increase of the reflection. That the absorption decreases with increasing excited carrier concentration can be seen from the fluence dependence in this study (see figure 3.22 in the appendix). Coherent lattice vibrations are also clearly observed as an oscillation in the differential reflection signal. This is an A_{1g} longitudinal optical phonon with a frequency of 2.167±0.002THz.

Fluence dependence The decay times in our experiment on thin film Bi_2Se_3 show to be on the same order of magnitude, but nevertheless ∼2x as fast as the data presented by Kumar et al. [26]. The sign of our differential signal disagrees with the sign presented in [26, 27], but agrees with the sign presented in [24]. The negative reflectivity change was also measured in the 1kHz regenerative amplifier set. A possible explanation for this observation lies in the fact that for the thin film sample the metallic surface state electron concentration is higher than the bulk electron concentration, as discussed in section 3.3. The pump pulse will decrease the amount of free-electrons in the surface state, hence decrease the metallicity. This will give a decrease in the reflection coefficient. As we do not have a bulk sample to compare our thin film sample with, this statement is still rather dubious.

The study in [26] shows that the decay constant stays approximately around ∼ 3.2ps over a

fluence range of 0-50μJ/cm^2. Our study clearly shows linear behaviour with increasing excited carrier concentration.

We were not able to clearly resolve the 2.167THz optical phonon in both the 80Mhz and 808kHz measurements. The cause of this is unknown.

Temperature dependence From the decay time versus temperature data presented in 3.23 it is clearly seen that the decay time increases with decreasing temperature. This can simply be explained by a lower phonon occupation number at lower temperatures. At low temperatures the excited carriers see fewer scattering objects (the phonons) hence the decay to the ground state takes a longer time.

3.5 Transient grating study

3.5.1 Transient grating setup

Transient grating technique In the transient grating method two crossed laser pulses create a spatial sinusoidal excitation pattern on a sample. The decay of this induced grating is monitored via diffraction of a probe pulse. Depending on the polarization of the incoming pulse beams the spatial pattern can either be an intensity grating or a polarization pattern.

In our experiment a phase mask is used which contains a variety of differently sized gratings. The groove spacing is defined as d. We use gratings with d varying from 10μm to 80μm. The grating is imaged onto the sample by an imaging system. The case where two convex lenses with the same focal lengths are used to obtain a 1:1 image system is drawn in figure 3.11.

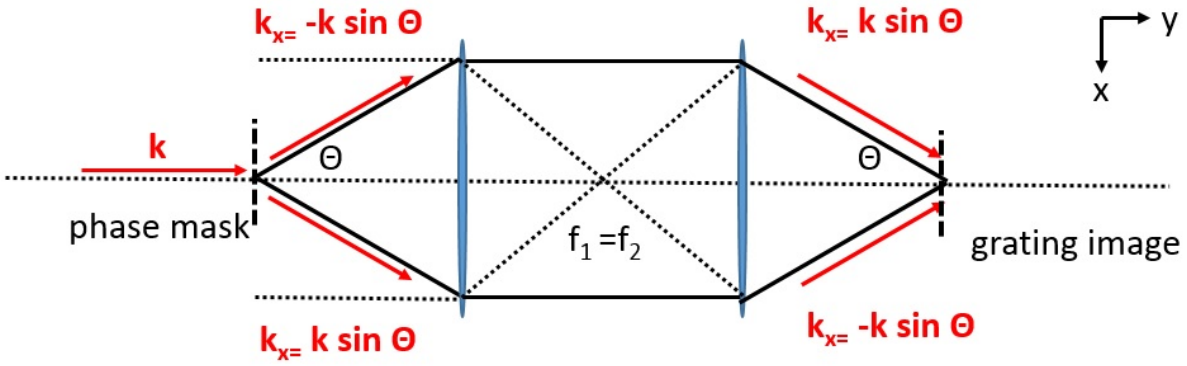

Figure 3.11: 1:1 imaging of a grating by means of two confocal mirrors with $f_1 = f_1$.

The angle θ is simply determined by the used wavelength λ, the groove spacing d and the diffraction condition $m\lambda = d \cdot \sin\theta$. Here m is the diffraction order. The first order diffraction signal is always used, so $m = \pm 1$. At the sample position the two electric fields add up. The electric field in the x-direction (along the grating) at the sample position can be expressed as:

$$E_{total} = E_0 e^{i\mathbf{k}_x\mathbf{x}} + E_0 e^{-i\mathbf{k}_x\mathbf{x}} = E_0 e^{i(k\sin\theta)\cdot x} + E_0 e^{-i(k\sin\theta)\cdot x} \tag{3.2}$$

Here $\mathbf{k}_x = k\sin\theta$ is the projection of the wavevector along the x-axis. The intensity can now be calculated as:

$$I \sim E_{total}^2 = 2(1 + \cos((2k\sin\theta)\cdot x)) \tag{3.3}$$

From this expression we see that we obtain a spatially modulated intensity pattern with a periodicity Λ given by:

$$\Lambda = \frac{2\pi}{2k\sin\theta} = \frac{\lambda}{2\sin\theta} = \frac{d}{2} \tag{3.4}$$

The last two expressions follow with k=$2\pi/\lambda$ and $m\lambda = d\cdot\sin\theta$. So a grating with groove size d sets up a spatial modulation with period $\Lambda = d/2$. The spatial intensity profile creates a spatially modulated transient carrier distribution $N(x,t) = N_0(t) + \Delta N(x,t)\cos((2k\sin\theta)\cdot x)$. Here N_0 is a uniform component and $\Delta N(x,t)$ the modulated part. In this way the refractive index is modulated, which is monitored by the diffracted probe beam.

The wavevector transfer corresponds to $\mathbf{q} = \Lambda/2\pi = 2k\sin\theta\mathbf{x}$. In this way the incoming beam $\mathbf{k}_x = -k\sin\theta\mathbf{x}$ *diffracts* into the direction $\mathbf{k} = -\mathbf{k}_x + \mathbf{q} = +k\sin\theta\mathbf{x}$. The *reflected* signal just propagates in the $\mathbf{k}_x = -k\sin\theta\mathbf{x}$ direction.

Monitoring both the differential reflection and diffraction signal allows to obtain the diffusion constant for a material. The reflection signal gives the electron-hole recombination time τ_R. The diffraction signal gives a decay rate $\Gamma = 1/\tau$ which consists of the recombination time plus a diffusion-related component. The expression for the decay rate Γ is [30]:

$$\Gamma = \frac{4\pi^2 D_a}{\Lambda^2} + \frac{1}{\tau_R} \tag{3.5}$$

Plotting the decay rate Γ versus Λ^{-2} allows to extract the ambipolar (electron-hole pairs are created upon laser excitation) diffusion coefficient.

Spin grating The above expressions are for incoming beams with *parallel* polarizations. When for one of the pump beams the polarization is rotated 90° (giving two orthogonal linearly polarized beams) by means of a $\lambda/2$-plate a *uniform* electric field is created, but the *helicity* is spatially modulated, as shown in figure 3.12. A linearly polarized probe beam will diffract from this spatial helicity modulation. The diffracted signal allows to obtain the *spin diffusion* coefficient D_s. The lifetime now is the electron spin relaxation time τ_s.

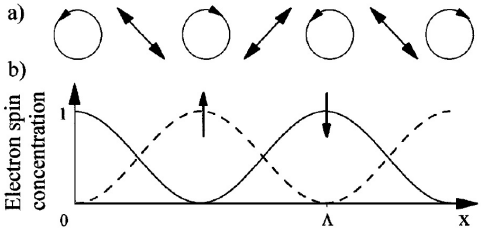

Figure 3.12: Two orthogonally oriented linearly polarized pump beams set up a polarization modulation. The lower graph gives the spin-up and spin-down concentration. Figure taken from [30].

Thermal grating As a last possibility the thermal grating is mentioned. Thermal processes happen on a timescale of $\sim$ 50ps to nanoseconds. As the pump intensity profile is spatially modulated, the absorption on the sample will also be spatially modulated. For the longer timescales this means that a heat profile is set up. Heat will diffuse into the sample with a characteristic timescale τ, which can be determined from the reflectivity. Heat also diffuses along the grating. A last possibility is that an oscillating signal is visible which originates from generated surface acoustic waves [31].

Our setup For the transient grating setup a 1kHz 800nm system based on a Ti:Sapphire oscillator with regenerative amplifier is used. After the beam splitter the pump beam is elevated 2 centimetres above the probe beam by a telescope. Both pump and probe beam are focussed on the phase mask. The first order diffracted beams are captured on a spherical mirror, which images the phase mask on the sample. The experimental geometry is drawn in figure 3.13. When the bottom right (probe) beam is blocked, the TG signal ends up in the lower detector and the transmission in the upper detector.

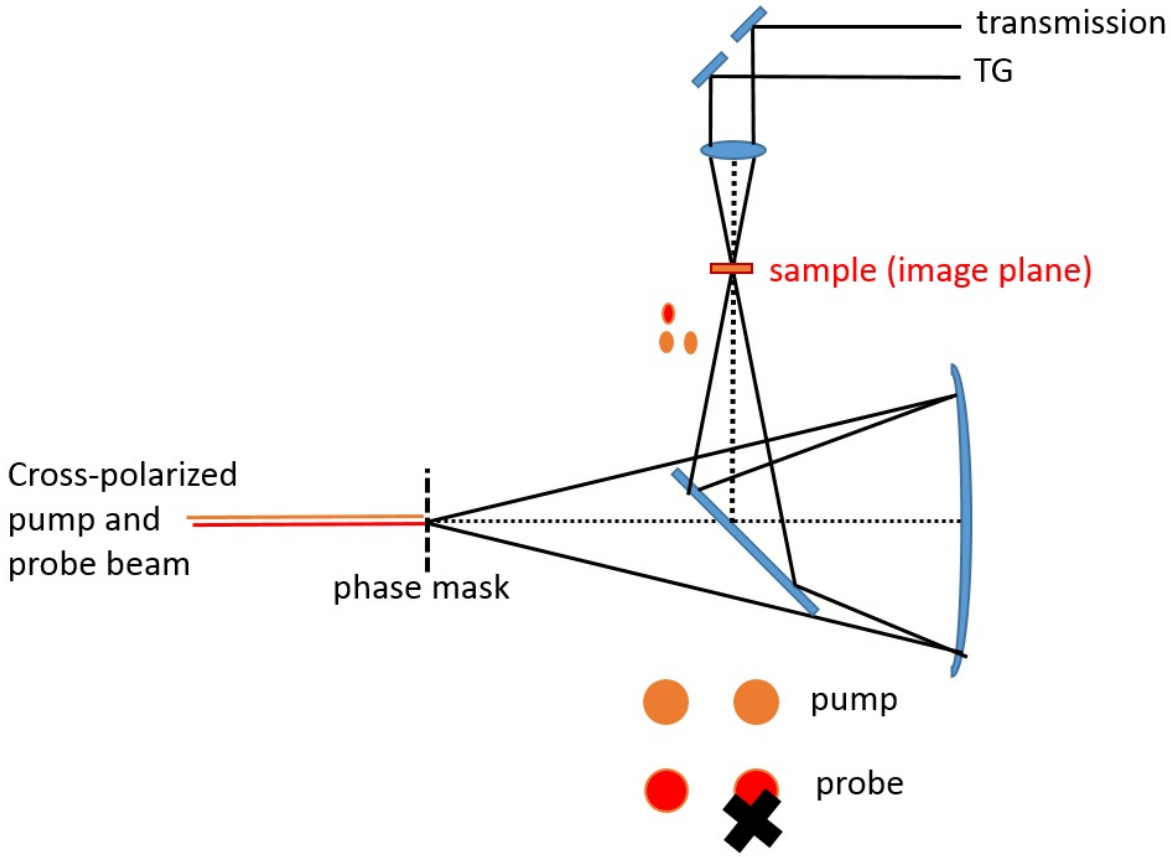

Figure 3.13: Overview of the transient grating setup. The pump and probe beam come in under a finite angle (in vertical direction) on the phase mask. The first order beams fall on the spherical mirror and image the grating at the sample. Two pump beams excite the sample and one probe beam is used. The reflected and diffracted signals end up in the detectors. The diffracted signal follows the same path as the blocked probe beam would follow, as explained in this section.

The smallest grating used has a physical grating size of d=10μm. Under 1:1 imaging conditions this sets up a grating of Λ=5μm on the sample. A spherical mirror is used to image the grating in our setup instead. Its curvature radius is R=505mm and the diameter is D=15cm. The physical bound to the object distance for this grating and spherical mirror diameter can be calculated with the grating equation $m\lambda = d \cdot \sin\theta$. So $\theta = \sin^{-1}(\lambda/d) = \sin^{-1}(800\text{nm}/10\mu\text{m})$=4,6°. With the radius r=7,5cm for the mirror this gives a maximum separation of l=7,5cm/tan 4, 6°$\sim$93cm. In order to be safe for spherical aberration problems we chose an image distance of $d_o\sim$77cm. The focal length F of the spherical mirror is given by $F = R/2$=252,5mm. This gives an image distance $d_i\sim$38cm. The magnification factor under these conditions is $m = d_i/d_o\sim$0,49. For the Λ=5μm phase mask this gives a grating of $\sim$2,5μm on the sample. This will be the smallest grating which can be realized in the setup.

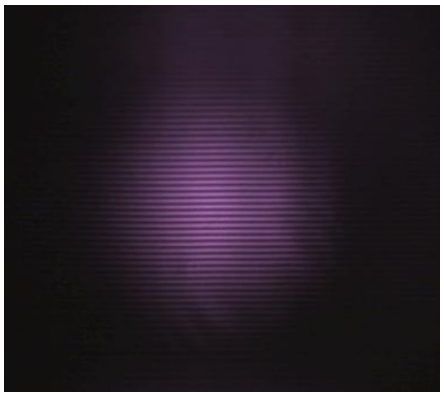

Figure 3.14: CCD-image of the imaged Λ=40μm grating.

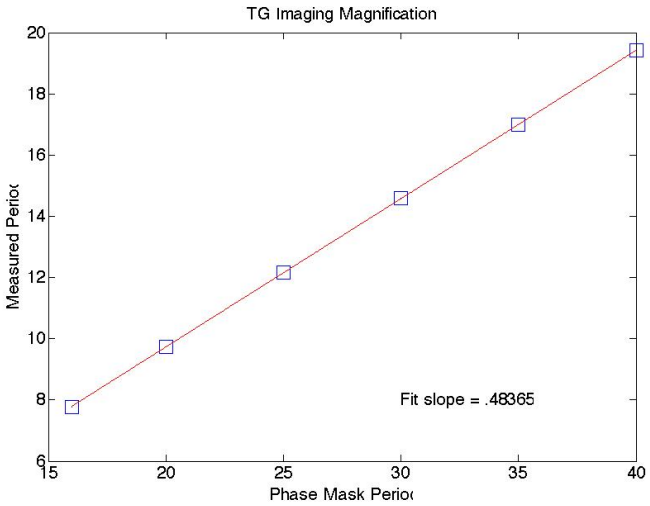

Figure 3.15: A phase mask Λ=d/2μm gives the following real space gratings on the sample.

The gratings varying from $\Lambda/2$=5μm to $\Lambda/2$=40μm are imaged on a CCD-camera. The center coordinates are determined with Gaussian fits and plotted versus grating periodicity in order to verify that the different gratings are imaged on the same spot on the sample. From this plot, presented in 3.16 it becomes clear that spherical aberration of the lens does not pose problems in the setup. The grating sizes as measured on the CCD-images versus phase mask indication are determined and plotted in graph 3.15.

3.5.2 Feasibility various diffusion processes

There are three diffusion processes in which we are interested. The "holy grail" is the spin diffusion described in section 3.2.2. The other two are the carrier diffusion process and the thermal diffusion process. Formula 3.5 allows to get an idea of the transient grating decay times $\tau = \Gamma^{-1}$ which need to be measured for the different processes.

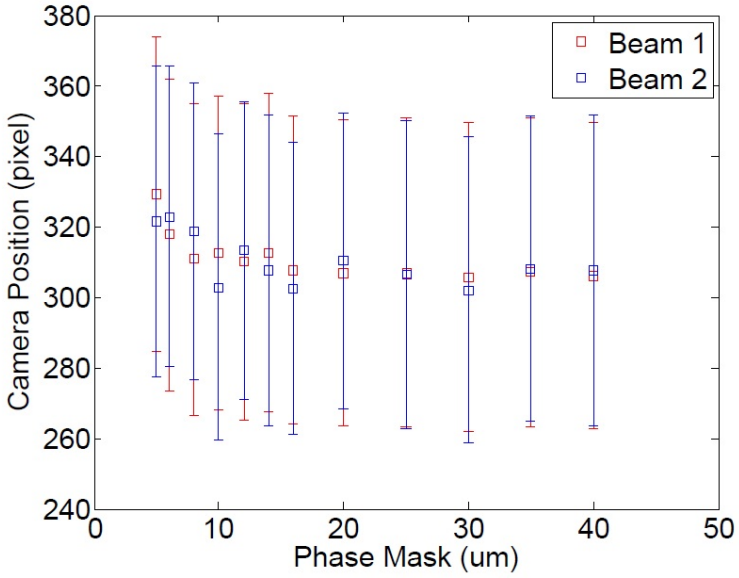

Figure 3.16: Position of left and right pump beam at the image position. Gratings are switched and the position is recorded. 1 pixel corresponds to 3.6μm.

Carrier diffusion

Reference [26] extracts a diffusion constant D_a=500cm^2/s. The recombination time is measured as τ_R ~3,2ps. As the amplifier setup produces higher fluences one can pick τ_R ~5,0ps for our case. The λ refers to the grating periodicity. When the gratings are changed from λ ~2,5μm to λ ~10μm we need to measure time constants from ~1,5ps to ~4,5ps, as can be seen from plot 3.17. This should be possible with our ~100fs time-resolution.

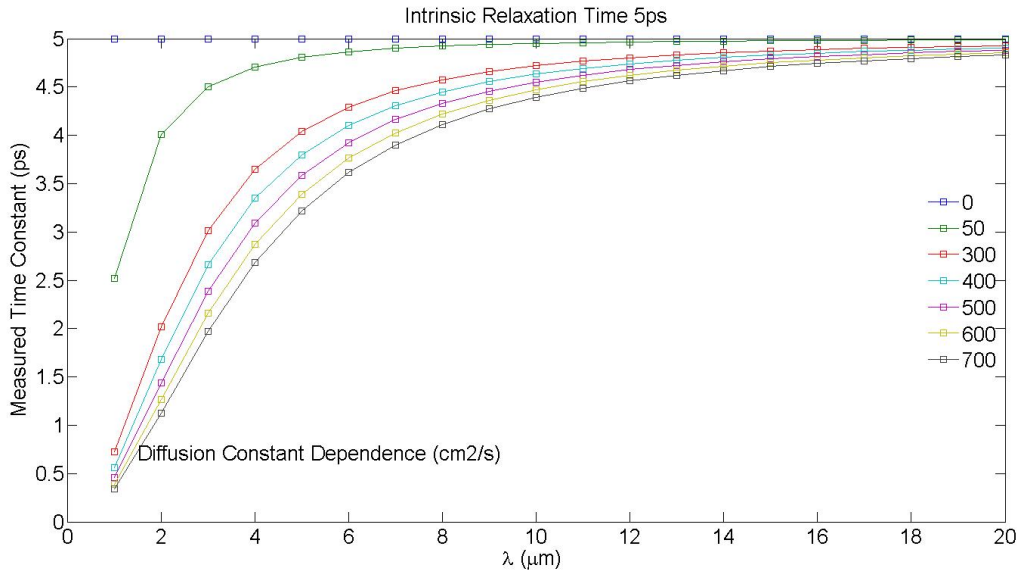

Figure 3.17: Expected graphs of grating periodicity versus measured decay times (in TG channel) for ambipolar diffusion. The different traces are for different ambipolar diffusion constants (indicated in cm^2/s). The used time τ_R ~5ps is indicative for the carrier relaxation.

Thermal diffusion

Reference [26] extracts a diffusion constant D_t=1,2cm^2/s for the thermal diffusion. We measure a recombination time on the order of τ_R ∼250ps for the thermal process. This recombination time corresponds to thermal diffusion *into* the plane, oppossed to along the grating. When the gratings are changed from λ ∼2,5μm to λ ∼10μm we need to discriminate between time constants of ∼200ps to ∼250ps, as can be seen from plot 3.18.

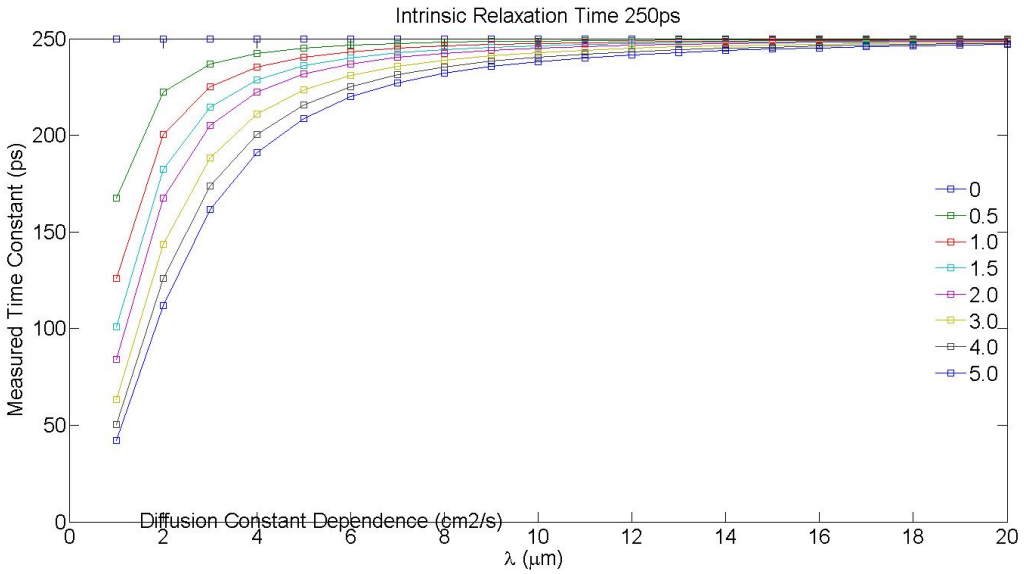

Figure 3.18: Expected graphs of grating periodicity versus measured decay times (in TG channel) for thermal diffusion. The different traces are for different thermal diffusion constants (indicated in cm^2/s). The used time τ_R ∼250ps is indicative for the thermal diffusion into the plane.

Spin diffusion

The feasibility of obtaining the spin diffusion constant by the transient grating technique is not possible for now, as relevant coefficients have not yet been determined by means of techniques such as spin-injection (as far as the author knows).

3.6 Conclusion

Carrier dynamics in a thin film of the 3D topological insulator Bi_2Se_3 have been studied. An ultrafast reflectivity setup with a time-resolution of $\tau \sim$ 33fs was constructed in order to obtain relaxation times. An ultrafast 1,5eV pump pulse is applied and the reflectivity change is monitored by a delayed 1,5eV probe pulse. The temperature dependence of the relaxation time τ_R shows that τ_R increases with decreasing temperature. This is in accordance with the fact that induced carriers observe less phonon scattering objects at lower temperatures. The fluence dependence shows that relaxation times increase with increasing induced carrier concentration.

In the transient grating experiment two 1,5eV pump pulses come in under the sample under a finite angle, setting up a spatially modulated intensity pattern. A delayed probe pulse measures the decay of the grating, giving information on relaxation *and* diffusion times in the sample. The setup was changed to an imaging system with a spherical mirror. The minimum grating which can be reliably obtained now is ∼2,5μm. The possibility to obtain diffusion constants for three

different physical processes, - carrier diffusion, spin diffusion and thermal diffusion -, was discussed. Carrier diffusion should very likely be possible to measure.

3.7 Appendix

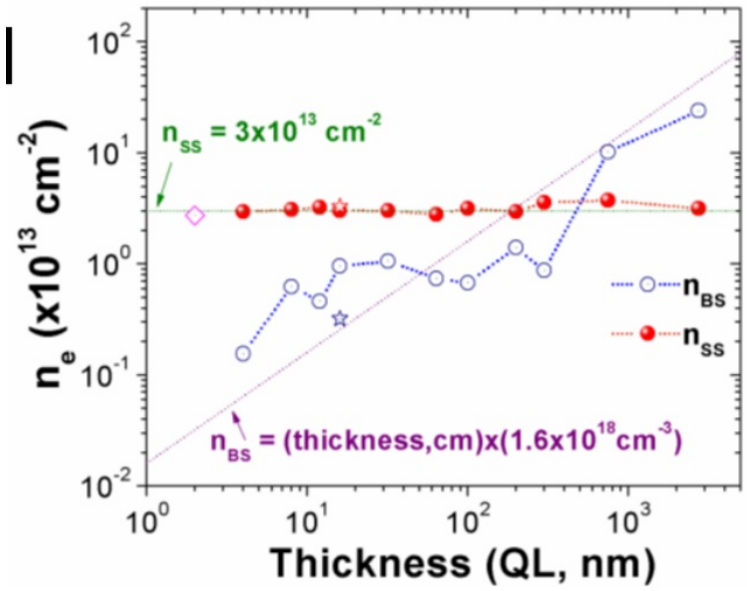

Figure 3.19: Carrier concentration versus amount of quintuple layers.

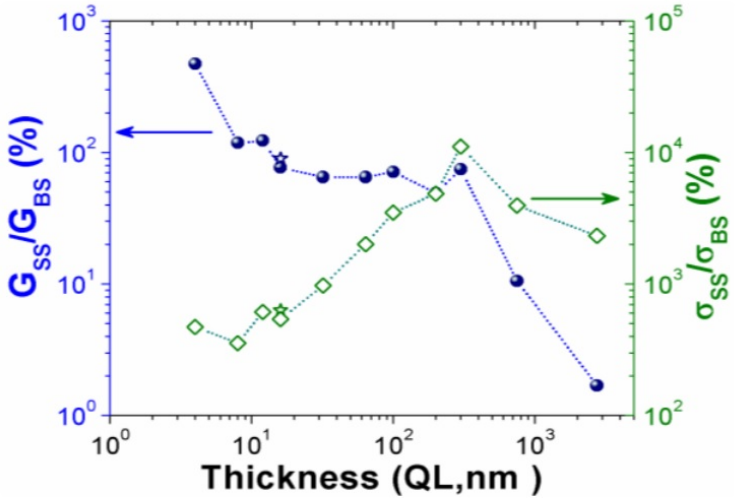

Figure 3.20: Conduction versus amount of quintuple layers.

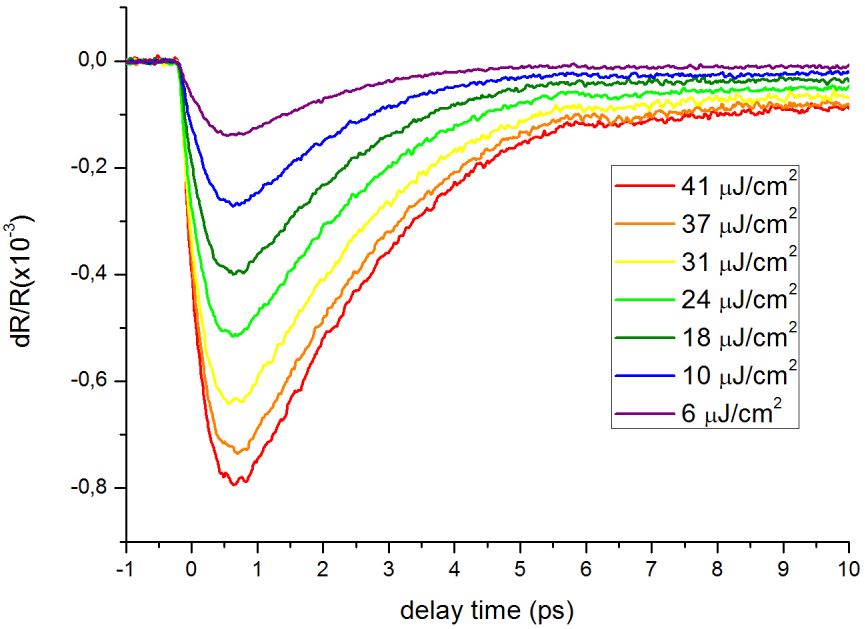

Figure 3.21: Differential signals of the fluence dependence study. Data was taken in cavity dumped mode. Clearly no coherent oscillations were resolved.

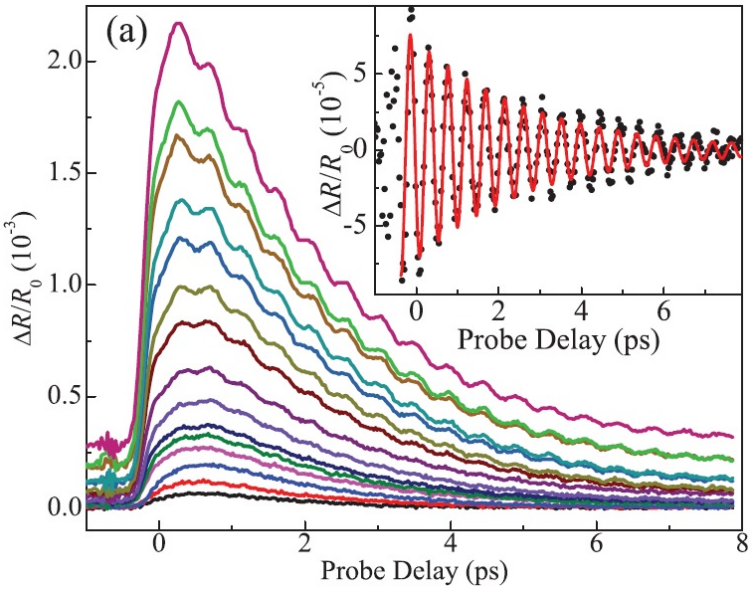

Figure 3.22: Fluence dependence of differential reflection on a single crystal Bi_2Se_3 sample from [26]. The fluence ranges from 3-50μJ/cm^2. Coherent lattice vibrations are clearly observed as an oscillation in the differential reflection signal.

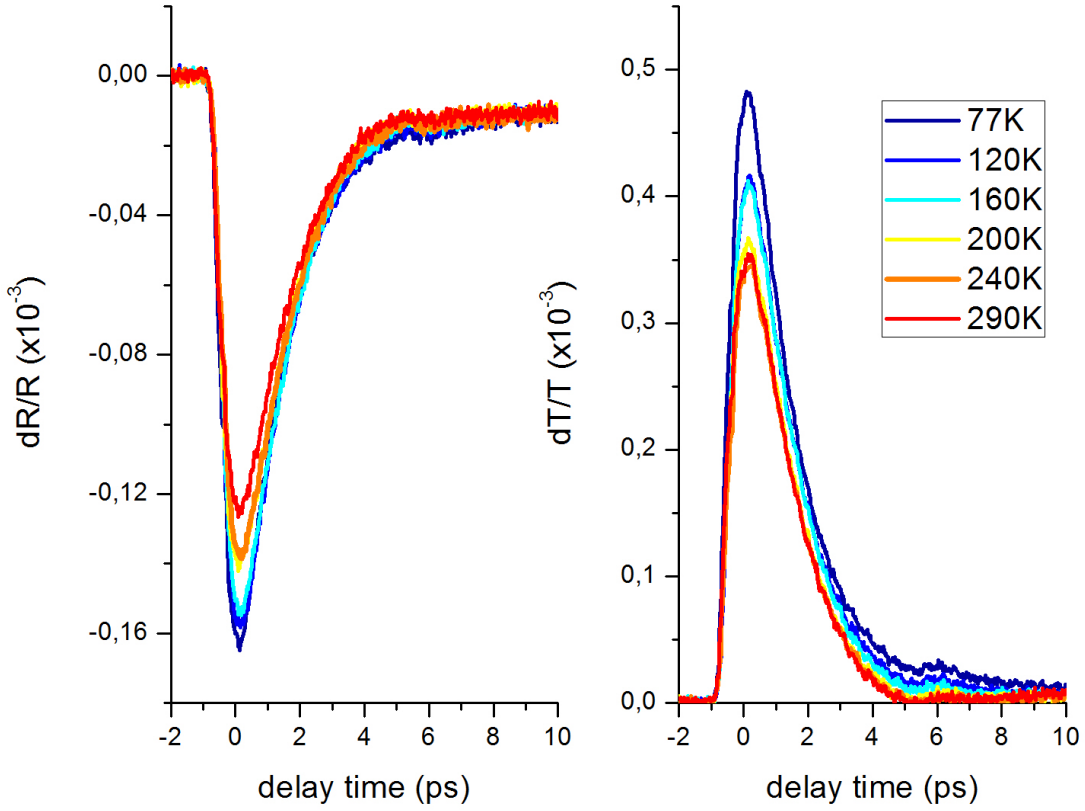

Figure 3.23: Temperature dependent differential traces. The left plot shows the change in reflectivity. The right plot shows the change in transmission.

Chapter 4

Acknowledgements

First of all I would like to thank Dr. Robert Schoenlein for giving me the opportunity to be a guest student in his group in the Fall period of 2012. I am really thankfull to Matt Langner and Yi Zhu for their splendid daily guidance over this period. I also would like to thank Yi-De Chuang for the nice scientific discussions and the time he spent to explain me interesting work in the oxide field. I would like to thank Jake Koralek for giving me the opportunity to work a few days at beamline 8. I should not forget to thank Dr. Sujoy Roy and Shrawan Mishra from the dysprosium-team.

For the research part performed in Groningen I would first of all like to thank Dr. Ron Tobey. I also would like to thank him for making the research opportunity in Berkeley possible. I also would like to thank Prof. Paul van Loosdrecht for making it possible being part of his ground and for all the scientific discussions we had. I should also thank Julius Janusosis and Qi Liu, who are also involved in the project. I want to thank Michiel Donker for learning me some things about magnetization dynamics. I also would like to thank the technicians Ben Hesp and Foppe de Haan and all the other people of the Optical Condensed Matter group for the nice time. Furthermore I would like to thank Dr. Graeme Blake for being part of the reading committee.

I would also like to thank the Stichting Hendrik Muller's Vaderlandsch Fonds, the Groninger Universiteitsfonds and the Marco Polo Fonds for providing me financial aide in realizing the interesting research opportunity in Berkeley.

Bibliography

[1] B. Koopmans, G. Malinowski, F. Dalla Longa, D. Steiauf, M. Faehnle, T. Roth, M. Cinchetti, and M. Aeschlimann. Explaining the paradoxical diversity of ultrafast laser-induced demagnetization. *Nature Materials*, 9(3):259–265, March 2010. 10.1038/NMAT2593.

[2] Jens Als-Nielsen and Des McMorrow. *Elements of Modern x-ray Physics*. Wiley, 2 edition, 2011.

[3] Y.D. Chuang, W.S. Lee, and et al. Phase fluctuations and the absence of topological defects in a photo-excited charge-ordered nickelate. *Nature Communications*, 3(838), may 2012. DOI: 10.1038/ncomms1837.

[4] S. Y. Zhou, Y. Zhu, M. C. Langner, Y.-D. Chuang, P. Yu, W. L. Yang, A. G. Cruz Gonzalez, N. Tahir, M. Rini, Y.-H. Chu, R. Ramesh, D.-H. Lee, Y. Tomioka, Y. Tokura, Z. Hussain, and R. W. Schoenlein. Ferromagnetic enhancement of ce-type spin ordering in PrCaMnO3. *Phys. Rev. Lett.*, 106:186404, May 2011.

[5] Brian W. J. McNeil and Neil R. Thompson. X-ray free-electron lasers. *Nature Photonics*, 4(12):814–821, 2010.

[6] Chan La-O-Vorakiat, Mark Siemens, Margaret M. Murnane, Henry C. Kapteyn, Stefan Mathias, Martin Aeschlimann, Patrik Grychtol, Roman Adam, Claus M. Schneider, Justin M. Shaw, Hans Nembach, and T. J. Silva. Ultrafast demagnetization dynamics at the M edges of magnetic elements observed using a tabletop high-harmonic soft x-ray source. *Phys. Rev. Lett.*, 103:257402, 2009.

[7] RW Schoenlein, S Chattopadhyay, HHW Chong, TE Glover, PA Heimann, CV Shank, AA Zholents, and MS Zolotorev. Generation of femtosecond pulses of synchrotron radiation. *Science*, 287(5461):2237–2240, Mar 2000.

[8] M Saes, C Bressler, F van Mourik, W Gawelda, M Kaiser, M Chergui, C Bressler, D Grolimund, R Abela, TE Glover, PA Heimann, RW Schoenlein, SL Johnson, AM Lindenberg, and RW Falcone. A setup for ultrafast time-resolved x-ray absorption spectroscopy. *Review of Scientific Instruments*, 75(1):24–30, Jan 2004.

[9] K Dumesnil, C Dufour, P Mangin, G Marchal, and M Hennion. Magnetic structure of dysprosium in epitaxial dy films and in dy/er superlattices. *Phys. Rev. B*, 54(9):6407–6420, Sep 1996.

[10] K.D. Jayasuriya, S.J. Campbell, and A.M. Stewart. Magnetic transitions in dysprosium - a specific-heat study. *PRB*, 31(9):6032–6046, 1985.

[11] S. Blundell. *Magnetism in Condensed Matter*. Oxford University Press, 2 edition, 2001.

[12] K. M. Dobrich, A. Bostwick, J. L. McChesney, K. Rossnagel, E. Rotenberg, and G. Kaindl. Fermi-surface topology and helical antiferromagnetism in heavy lanthanide metals. *Phys. Rev. Lett.*, 104:246401, Jun 2010.

[13] S. C. Keeton and T. L. Loucks. Electronic structure of rare-earth metals. i. relativistic augmented-plane-wave calculations. *Phys. Rev.*, 168:672–678, Apr 1968.

[14] Jens Jensen and Allan R. Mackintosh. *Rare Earth Magnetism - Structures and Excitations*. Clarendon Press Oxford, 1991.

[15] C. Stamm, T. Kachel, N. Pontius, R. Mitzner, T. Quast, K.Holldak, S.Khan, C.Lupulescu, E.F. Aziz, M. Wietstruk, H.A Durr, and W. Eberhardt. Femtosecond modification of electron localization and transfer of angular momentum in nickel. *Nature Materials*, 6(10):740–743, October 2007. DOI: 10.1038/nmat1985.

[16] G.M. Mueller. Spin polarization in half-metals probed by femtosecond spin excitation. *Nature Materials*, 8(1):56–61, december 2008. DOI: 10.1038/NMAT2341.

[17] Marko Wietstruk, Alexey Melnikov, Christian Stamm, Torsten Kachel, Niko Pontius, Muhammad Sultan, Cornelius Gahl, Martin Weinelt, Hermann A. Durr, and Uwe Bovensiepen. Hot-electron-driven enhancement of spin-lattice coupling in gd and tb $4f$ ferromagnets observed by femtosecond x-ray magnetic circular dichroism. *Phys. Rev. Lett.*, 106:127401, Mar 2011.

[18] A. J. Schellekens and B. Koopmans. Microscopic model for ultrafast magnetization dynamics of multisublattice magnets. *Phys. Rev. B*, 87:020407, Jan 2013.

[19] L.P. Kouwenhoven, V. Mourik, K. Zuo, S. M. Frolov, S. R. Plissard, and E. P. A. M. Bakkers. Signatures of Majorana Fermions in Hybrid Superconductor-Semiconductor Nanowire Devices. *Science*, 10.1126/science.1222360, 2012.

[20] Joel E. Moore. The birth of topological insulators. *Nature*, 464(7286):194–198, Mar 2010.

[21] M. Z. Hasan and C. L. Kane. Colloquium: Topological insulators. *Reviews of Modern Physics*, 82(4):3045–3067, Nov 2010.

[22] Haijun Zhang, Chao-Xing Liu, Xiao-Liang Qi, Xi Dai, Zhong Fang, and Shou-Cheng Zhang. Topological insulators in Bi_2Se_3, Bi_2Te_3 and Sb_2Te_3 with a single dirac cone on the surface. *Nature Physics*, 5(6):438–442, Jun 2009.

[23] Lukas Muechler, Frederick Casper, Binghai Yan, Stanislav Chadov, and Claudia Felser. Topological insulators and thermoelectric materials.

[24] D. Hsieh, F. Mahmood, J. W. McIver, D. R. Gardner, Y. S. Lee, and N. Gedik. Selective probing of photoinduced charge and spin dynamics in the bulk and surface of a topological insulator. *Phys. Rev. Lett.*, 107:077401, Aug 2011.

[25] J. A. Sobota, S. Yang, J. G. Analytis, Y. L. Chen, I. R. Fisher, P. S. Kirchmann, and Z.X. Shen. Ultrafast optical excitation of a persistent surface-state population in the topological insulator Bi_2Se_3. *Phys. Rev. Lett.*, 108:117403, Mar 2012.

[26] Nardeep Kumar, Brian A. Ruzicka, N. P. Butch, P. Syers, K. Kirshenbaum, J. Paglione, and Hui Zhao. Spatially resolved femtosecond pump-probe study of topological insulator Bi_2Se_3. *Phys. Rev. B*, 83:235306, Jun 2011.

[27] J. Qi, X. Chen, W. Yu, P. Cadden-Zimansky, D. Smirnov, N. H. Tolk, I. Miotkowski, H. Cao, Y. P. Chen, Y. Wu, S. Qiao, and Z. Jiang. Ultrafast carrier and phonon dynamics in Bi_2Se_3 crystals. *Applied Physics Letters*, 97(18), Nov 2010.

[28] N. Bansal, Y.S. Kim, M. Brahlek, E. Edrey, and S. Oh. Giant surface transport in topological insulator Bi_2Se_3 thin films. *preprint*.

[29] Yi Zhang, Ke He, Cui-Zu Chang, Can-Li Song, Li-Li Wang, Xi Chen, Jin-Feng Jia, Zhong Fang, Xi Dai, Wen-Yu Shan, Shun-Qing Shen, Qian Niu, Xiao-Liang Qi, Shou-Cheng Zhang, Xu-Cun Ma, and Qi-Kun Xue. Crossover of the three-dimensional topological insulator Bi_2Se_3 to the two-dimensional limit. *Nature physics*, 6(8):584–588, Aug 2010.

[30] A. R. Cameron, P. Riblet, and A. Miller. Spin gratings and the measurement of electron drift mobility in multiple quantum well semiconductors. *Phys. Rev. Lett.*, 76:4793–4796, Jun 1996.

[31] Jeremy A. Johnson, Alexei A. Maznev, Mayank T. Bulsara, Eugene A. Fitzgerald, T. C. Harman, S. Calawa, C. J. Vineis, G. Turner, and Keith A. Nelson. Phase-controlled, heterodyne laser-induced transient grating measurements of thermal transport properties in opaque material. *Journal of Applied Physics*, 111(2), Jan 2012.